Medición del tiempo de vida media del meson B_s en el experimento DØ

Pedro Luis Manuel Podesta Lerma

Octubre 7 2006

Esta tesis fué realizada con el apoyo económico del Consejo Nacional de Ciencia y Tecnología (CONACYT), del Centro de Investigacion y Estudios Avanzados del IPN (CINVESTAV), del Sistema Nacional de Investigadores (SNI) y del Fermi National Accelerator Laboratory (FERMILAB).

Resumen

Usando el decaimiento exclusivo $B_s \to J/\psi(\mu^+\mu^-)\phi(K^+K^-)$, realizamos la medición del tiempo de vida media del mesón B_s . Los datos corresponden a una luminosidad integrada de aproximadamente 220 pb^{-1} obtenidos con el detector DØ en Fermilab durante el periodo 2002–2004. Reconstruimos 337 candidatos a B_s, con los cuales medimos:

$$\tau(B_s) = 1.444^{+0.098}_{-0.090}(\mathrm{stat}) \pm 0.020(\mathrm{sys})\ \mathrm{ps}.$$

También obtuvimos el tiempo de vida media del mesón B_d usando el decaimiento exclusivo $B_d \to J/\psi(\mu^+\mu^-)K^{*0}(892)(K^+\pi^-)$. De 1370 candidatos reconstruidos medimos:

$$\tau(B_d) = 1.473^{+0.052}_{-0.050}(\mathrm{stat}) \pm 0.023(\mathrm{sys})\ \mathrm{ps}.$$

Combinando ambas mediciones obtuvimos la razón de los tiempos de vida media:

$$\tau(B_s)/\tau(B_d) = 0.980^{+0.076}_{-0.071}(\mathrm{stat}) \pm 0.003(\mathrm{sys}).$$

La cual concuerda con la predicción de la teoría efectiva de quarks pesados donde la diferencia es de solo 1%.

Abstract

Using the exclusive decay $B_s \to J/\psi(\mu^+\mu^-)\phi(K^+K^-)$, we measured the average lifetime of the B_s mesons. The data correspond to an integrated luminosity of approximately 220 pb^{-1} obtained in the DØ detector at Fermilab during the period 2002–2004. We reconstruct 337 B_s candidates, from which we got:

$$\tau(B_s) = 1.444^{+0.098}_{-0.090}(\mathrm{stat}) \pm 0.020(\mathrm{sys})\ \mathrm{ps}.$$

We also measured the average lifetime of the B_d meson using the exclusive decay $B_d \to J/\psi(\mu^+\mu^-)K^{*0}(892)(K^+\pi^-)$. From 1370 candidates reconstructed we measured:

$$\tau(B_d) = 1.473^{+0.052}_{-0.050}(\mathrm{stat}) \pm 0.023(\mathrm{sys})\ \mathrm{ps}.$$

Combining both measurements we calculated the ratio of the average lifetimes to be:

$$\tau(B_s)/\tau(B_d) = 0.980^{+0.076}_{-0.071}(\mathrm{stat}) \pm 0.003(\mathrm{sys}).$$

The measured ratio is in agreement with the heavy quark expansion theory where the difference is just 1%.

Agradecimientos

Me gustaría agradecer a tantas personas dado que este trabajo fue el resultado de una colaboración internacional, así cientos si no es que miles de individuos contribuyerón a el. Primero agradezco el apoyo de mi familia, de mi esposa Reyna, mis padres y mis hermanos. Agradezco a mis asesor Alberto Sánchez por haberme guiado en este campo lleno de tantos recovecos como es la física experimental de altas energias, a Heriberto Castilla que me apoyo incondicionalmente durante mi estancia de 3 años en Fermilab.

A mi compañero Eduard de La Cruz con quien discutí muchos aspectos de esta tesis, a mis amigos de Fermilab Juan Estrada, Jorge Molina, Ricardo Ramirez, Sarosh Fatakia, Martin Maekler y Sebastian Carron que me hicieron muy llevadera la estancia en el laboratorio.

A Guennadi Borissov cuyo programa de vertices fue un factor importante en este analisis. A Rick Van Kooten quin sugirio varios chequeos, a Brendan Casey quien me ayudo en este análisis y con quien realizé el análisis del B cargado justo al empezar mi doctorado.

Agradezco al consejo editorial de DØ compuesto por Ron Lipton, Daniela Bauer, John Parsons, Eckhard von Toerne, Phil Gutierrez por su revisión y ayuda en la publicación del artículo reultado de esta tesis.

También agradezco la ayuda del Jianming Quian quien fungió como coordinador de resultados de física y en especial a Gene Fisk por su apoyo económico a traves de Fermilab.

A Markus Wobish y Dimitri Denissov por su ayuda mis turno de vigilar el sistema de muones. También agradezco a Brandy Meyers que ma auxilió en todo el engorroso tramite de visas.

Agradezco a todos mis maestros que compartieron su conocimentos conmigo y a mis amigos de CINVESTAV Ramon Castañeda, Armando Pérez, Paty Pliego, Imelda Galaviz, Americo Rodriguéz, Hernan Herrera y Alex Forido.

A Reyna y Handel con amor.

Contents

List of Tables

List of Figures

Chapter 1

Theoretical Background

1.1 Introduction

The Standard Model (SM) is a theoretical framework built from observations that predict and correlates new data. In the early 1960's particle physicist described nature in terms of four distinct forces, characterized by widely different spatial ranges and strengths as measured at typical energy scale of 1 GeV. The strong nuclear force has a range of about a Fermi or 10^{-15} m. The weak force responsible for radioactive decay, with a range of 10^{-7} m, is about 10^{-5} times weaker at this low energy. The electromagnetic force that governs much of the macroscopic physics has an infinite range and strength determined by the fine structure constant, $\alpha \approx 10^{2}$. The fourth force, gravity, also has infinite range and a low energy coupling (about 10^{-40}) too weak to be observable in laboratory experiments. The achievement of the SM was the elaboration of a unified description of the strong, weak and electromagnetic forces in the language of quantum gauge field theories. Moreover, the SM combines the weak and electromagnetic forces in a single electroweak gauge theory, reminiscent of Maxwell's unification of the seemingly distinct forces of electricity and magnetism.

By mid-century, the electromagnetic force was well understood as a renormalizable quantum field theory(QFT) known as quantum electrodynamics or QED. 'Renormalizable' means that once a few parameters are determined by a limited set of measurements, the quantitative features of interactions among charged particles and photons can be calculated to arbitrary accuracy as a perturbative expansion in the fine structure constant. QED has been tested over an energy range from 10^6 eV to tens of GeV,*i.e.* distances ranging from 10^{-11} m to 10^{-17} m. In contrast, the nuclear force was characterized by a coupling strength that precluded a perturbative expansion. Moreover, couplings involving higher spin states (resonances), that appeared to be on the same footing as nucleons or pions particle's, could not be described by a renormalizable theory, nor could the weak interactions that were attributed to the direct coupling of four fermions to one another.

1.2 Standard Model

The SM is characterized in part by the spectrum of elementary fields shown in Table 1.2 extracted from [2]. The matter fields are fermions and their anti-particles, with half unit of intrinsic angular momentum or spin. There are three families of fermions fields that are identical in every attribute except in their masses. (In table 1.2 one family per row) The first family includes the up(u) ad down (d) quarks that are the constituents of nucleons as well as pions an other mesons responsible for nuclear binding. It also contains the electron and the neutrino emitted with a positron in nuclear β-decay. The second family correspond to the charm(c) and down (d) quarks . It also contains the leptons muon(μ) and neutrino of the muon(ν_μ) muon(μ) decay spontaneously to electron neutrinos an other particles. The mean lifetime of the muon is $2.2 times 10^6 s$. The third family is composed of the top(t) and bottom(d) quarks the physics involving this quarks has just been investigated in the past two decades, the leptons are the charged bosons $W^\pm$ and the neutral boson Z^0 this interactions are typified by the slow process of nuclear β-decay their masses are of the order of 100 times the proton mass.

The spin-1 gauge boson mediate interactions among fermions. In QED, interactions among electrically charged particles are due to the exchange of quanta of the electromagnetic field called photons (γ). The fact that the γ is massless accounts for the long range of

QUARKS: $S = \frac{1}{2}$				LEPTONS: $S = \frac{1}{2}$				GAUGE BOSONS: $S = 1$	
$Q = \frac{2}{3}$	m	$Q = -\frac{1}{3}$	m	Q=-1	m	Q=0	m	quanta	m
$u_1\ u_2\ u_3$	(2–8)10^{-3}	$d_1\ d_2\ d_3$	(5–15)10^{-3}	e	5.11×10^{-4}	ν_e	$< 1.5 \times 10^{-8}$	$g_1 \cdots g_8$	$<$ a few $\times 10^{-3}$
$c_1\ c_2\ c_3$	1.0–1.6	$s_1\ s_2\ s_3$	0.1–0.3	μ	0.10566	ν_μ	$< 1.7 \times 10^{-4}$	γ	$< 6 \times 10^{-25}$
$t_1\ t_2\ t_3$	173.8±5.0	$b_1\ b_2\ b_3$	4.1–4.5	τ	1.7770	ν_τ	$< 1.8 \times 10^{-2}$	$W^\pm, Z^0$	80.39±0.06,91.187±0.002

Table 1.1: Elementary particles of the SM: $S(\hbar)$ is spin, $Q(e)$ is electric charge, and $m(\mathrm{GeV}/c^2)$ is mass. Numerical subscripts indicate the distinct color states of quarks and gluons. Each row correspond to a different family.

electromagnetic force. The strong force which is taken into account by quantum chromodynamics or QCD, is mediated by the exchange of massless gluons (g) between quarks that carry a quantum number called color. In contrast to the electrically neutral photon, gluons posses color charge and hence couple to one another. As a consequence, the color force between two colored particles increases in strength with increased distance. Thus quarks and gluons cannot appear as free particles, but exist only inside composite particles, called hadrons, with no net color charge. Nucleons are composed of three quarks of different colors, resulting in a 'white' color neutral state. Mesons contains quark and anti-quark pairs whose color charges cancel. Since a gluon inside a nucleon cannot escape its boundaries, the nuclear force is mediated by color-neutral bound states, accounting for its short range. This spacial range is characterized by the Compton wavelength of the lightest of these ($\approx 135 MeV$): the π-meson.

The even shorter range of the weak force is associated with the Compton wave-lengths of the charged W an neutral Z bosons that mediate it. The couplings of the bosons to the "weak charges" of quarks and leptons are comparable in strength to the electromagnetic coupling. When the weak interaction is measured over distances much larger than its range, its effects are averaged over the measurement area and hence suppressed in amplitude by a factor $(E/M_{W,Z})^2 \approx (E/100GeV)^2$, where E is the characteristic energy transfer in the measurement. Because the W particles carry electric charge they must couple to the γ, implying a gauge theory that unites the weak and electromagnetic interactions, similar to QCD in that the gauge particles are self coupled. In distinction to γ's and gluons, W's couple only to left-handed fermions (with spin oriented opposite to the direction of motion).

The SM is further characterized by a high degree of symmetry. For example, one cannot perform an experiment that would distinguish the color of the quarks involved. If the symmetries of the SM coupling were fully respected in nature, we would not distinguish an electron from neutrino or a proton from a neutron; their detectable differences are attributed to 'spontaneous' breaking of the symmetry. Just as the spherical symmetry of the earth is broken to a cylindrical symmetry by the earth's magnetic field, a field permeating all space, called the Higgs field, is invoked to explain the observation that the symmetries of electroweak theory are broke into the residual gauge symmetry of QED. Particles that interact with the Higgs field cannot propagate at the speed of light, and acquire masses, in analogy to the index of refraction that slows down a photon traversing matter. Particles that do not interact with the Higgs field namely the photon and gluons remain massless. Fermions couple to the Higgs field not only to determine their masses; the fermions induce a misalignment of quark mass eigenstates with the eigenstates of the weak charges, thereby allowing all fermions of heavy families to decay to lighter ones. These couplings provide the only mechanism within the SM that can account for the observed violation of CP, that is, invariance of the laws of nature under mirror reflection (parity P) and interchange of particles with their anti-particles (charge conjugation C).

The origin of the Higgs field has not yet been determined. However our very understanding of the SM implies that physics associated to electroweak symmetry breaking (ESB) must become manifest at energies present at Tevatron or at LHC under construction. There is a strong evidence stemming from quantum instability of scalar masses meaning the vast range of the mass scale, to believe that physics will point out to a modification of the theory. One shortcoming of the SM is it failure to include gravity. For which there is no renormalizable QFT because of the gravitational field boson has two units of spin. Experiments probing higher energies and shorter distances may reveal clues connecting SM physics to gravity, and may shed light on to other question presently unanswered.

1.3 CP Violation

Symmetries and their conservation laws form, together with the elementary particles and their interactions, the basis of the fundamental physical description of nature. Until approximatively 1956 it was assumed that the laws of physics remain unchanged when one changes the sign of spatial coordinates (i.e. changing x, y or z into -x, -y or -z) in a given system. This mirroring is called the parity operation P. However, C.S. Wu observed that the mirror image of the left-handed neutrino to be the right-handed neutrino, does not exist and that therefore the symmetry of the weak interaction is broken by the P operation. The symmetry is restored when the P operator is not applied alone, but when the combined operation CP is applied. C (charge conjugation) is the operation that transforms a particle into its anti-particle. CP-transformation transforms a left-handed neutrino into a right-handed anti-neutrino, which does exist.

In 1964, a symmetry violation of the CP-transformation was observed by James Cronin and Val Fitch in the case of the neutral K-meson at a level of 0,2%. Since then accurate measurements have taken place to determine the origin of CP violation in the K-meson system. However, in the K-meson system, such effects due to the strong interaction are too large to lead to any conclusion about the origin of CP violation. The expectation is that these effects will be less and better to determine in the case of a heavier meson such as the B-meson.

The question is now why the universe exists out of matter and not out of antimatter. (Experimentally we are sure that less than 0.01% of the universe consists out of antimatter). Indeed, in all reactions that we know of where a quark is produced, an anti-quark is also produced. This asymmetry is the result of CP-violation.

1.4 CKM Matrix

In the SM the quark eigenstates are not the same as the weak eigenstates, and the matrix relating these bases was defined for six quarks, Its explicit parametrization was given by

Kobayashi and Maskawa [3] in 1973 . This generalize the four-quark case, where the matrix is described by a single parameter, the Cabibbo angle [4].

By convention, the mixing is often expressed in terms of a 3×3 unitary matrix V operation on the charge -$e/3$ quark mass eigenstates (d,s and b) :

$$\begin{pmatrix} d' \\ s' \\ b' \end{pmatrix} = \begin{pmatrix} V_{ud} & V_{us} & V_{ub} \\ V_{cd} & V_{cs} & V_{cb} \\ V_{td} & V_{ts} & V_{tb} \end{pmatrix} \begin{pmatrix} d \\ s \\ b \end{pmatrix} \tag{1.1}$$

There are several parameterizations of the Cabibbo-Kobayashi-Maskawa (CKM) matrix. We advocate a "standard" parametrization [5] of V that utilizes angles $\theta_{12}, \theta_{23}, \theta_{13}$ and a phase δ_{13}

$$V = \begin{pmatrix} c_{12}c_{13} & s_{12}c_{13} & s_{13}e^{-i\delta_{13}} \\ -s_{12}c_{23} - c_{12}s_{23}s_{13}e^{i\delta_{13}} & c_{12}c_{23} - s_{12}s_{23}s_{13}e^{i\delta_{13}} & s_{23}c_{13} \\ s_{12}s_{23} - c_{12}s_{23}s_{13}e^{i\delta_{13}} & -c_{12}s_{23} - s_{12}s_{23}s_{13}e^{i\delta_{13}} & c_{23}c_{13} \end{pmatrix}, \tag{1.2}$$

with $c_{ij} = cos\theta_{ij}$ and $s_{ij} = sin\theta_{ij}$ for the "generation" labels $i, j = 1, 2, 3$. This has distinct advantages of interpretation, for the rotation angles are defined and labeled in a way which relates to the mixing of two specific generations, and if one of these angles vanishes, so does the mixing between those two generations; in the limit $\theta_{23} = \theta_{13} = 0$, the third generations decouples, and the situation reduces to the usual Carbon mixing of the first two generations, with θ_{12} identified as the Cabibbo angle. The real angles $\theta_{12}, \theta_{23}, \theta_{13}$ can all be made to lie in the first quadrant by the appropriate redefinition of quark field phases.

The matrix elements in the first and third row, which have been directly measured in decay processes, are all of a simple form, and c_{13} is know to deviate from unity in the sixth decimal place, $V_{ud} = c_{12}, V_{us} = s_{12}, V_{ub} = s_{13}e^{-i\delta_{13}}, V_{cb} = s_{23}$ and $V_{tb} = c_{23}$ to an excellent approximation. The phase δ_{13} lies in $0 \leq \delta 13 < 2\pi$, with non-zero values generally breaking CP invariance for the weak interactions.

The standard parametrization can be approximated in a way that emphasizes the hier-

Parameter	value	Extracted
$\|V_{ud}\|$	0.9734 ± 0.0008	Beta Decay
$\|V_{us}\|$	0.2196 ± 0.0026	K Decay
$\|V_{cd}\|$	0.224 ± 0.0016	$\nu\bar{\nu}$ production
$\|V_{cs}\|$	0.996 ± 0.013	ν production and semileptonic Decay
$\|V_{cb}\|$	$(41.2 \pm 2.0) \times 10^{-3}$	B Decays
$\|V_{ub}\|$	$(3.6 \pm 0.7) \times 10^{-3}$	B Decays
$\frac{\|V_{tb}\|^2}{\|V_{td}\|^2+\|V_{td}\|^2+\|V_{tb}\|^2}$	$0.94 + 0.31 - 0.24$	Top Decay

Table 1.2: CKM values

archy in the size of the angles, $s_{12} \gg s_{23} \gg s_{13}$ [6], known as Wolfeinstein parametrization. Setting $\lambda \equiv s_{12}$, the sine of the Cabibbo angle, one expresses the other elements in the terms of powers of λ:

$$V = \begin{pmatrix} 1-\lambda^2/2 & \lambda & A\lambda^3(\rho - i\eta) \\ -\lambda & 1-\lambda^2/2 & A\lambda^2 \\ A\lambda^3(1-\rho-i\eta) & A\lambda^2 & 1 \end{pmatrix}, +O(\lambda^4) \tag{1.3}$$

with A, ρ and η real numbers that were intended to be of the order of the unity. This form is widely used, especially for B physics, but care must be taken, especially for CP-violating effects in K physics, since the phase entering in V_{cd} and V_{cs} terms are higher order in λ.

The unitarity of the CKM matrix could be corroborated experimentally and hence give us physics beyond SM, some of which parameters have been measured and are resumed in table 1.2 taken from [7]. The unitarity is still not fully established.

Direct and indirect information on the smallest matrix elements of the CKM matrix is neatly summarized in terms of the "unitary triangle", one of six such triangles that correspond to the unitarity condition applied to two different rows or columns of the CKM matrix. Unitarity applied to the first and third column yields

$$V_{ud}V_{ub}^* + V_{cd}V_{cb}^* + V_{td}V_{tb}^* = 0. \tag{1.4}$$

The unitarity triangle is just a geometrical presentation of this equation in the complex

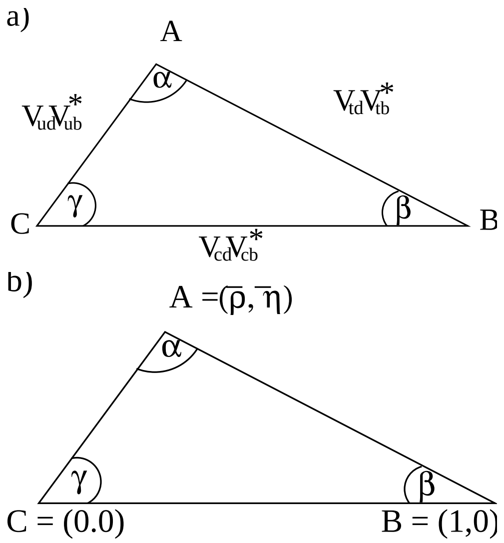

Figure 1.1: (a) Representation in the complex plane of the triangle formed by the CKM matrix elements $V_{ud}V_{ub}^*$, $V_{td}V_{tb}^*$, and $V_{cd}V_{cb}^*$. (b) Rescaled triangle with vertices A,B, and C at $(\bar{\rho}, \bar{\eta})$, $(1, 0)$ and $(0, 0)$ respectively.

plane, as in Figure 1.1 (a). We can always choose to orient the triangle so that $V_{cd}V_{cd}^*$ lies along the horizontal; in the standard parametrization, V_{cb} is real and V_{cd} is real to a very good approximation in any case. Setting cosines of small angles to unity Equation 1.4 becomes:

$$V_{ub}^* + V_{td} = s_{12}V_{cb}^*. \tag{1.5}$$

Which is shown as the unitarity triangle. The sides of this triangle are of the order 1% of the diagonal elements of the CKM matrix, which highlights the precision we are aiming to achieve when knowing each of these sides in turn to a precision of a few percent.

The angle α, β and γ of the triangle are also referred to as ϕ_2, ϕ_1 and ϕ_3 respectively with β and $\gamma = \delta_{13}$ being the phases of the CKM elements V_{td} and V_{ub} as per

$$V_{td}^* = |V_{td}|e^{-i\beta}, V_{ub} = |V_{ub}|e^{-i\gamma} \tag{1.6}$$

Rescaling the triangle so that the base is of unit length, the coordinates of the vertices A,B, and C becomes respectively:

$$(Re(V_{ud}V_{ub}^*)/|V_{cd}V_{cb}^*|, Im(V_{ud}V_{ub}*)/|V_{cd}V_{cb}*|), (1,0) \text{and} (0,0). \tag{1.7}$$

The coordinates of the apex of the rescaled unitarity triangle take the simple form $(\bar{\rho}, \bar{\eta})$ with $\bar{\rho} = \rho(1 - \lambda^2/2)$ and $\bar{\eta} = \eta(1 - \lambda^2/2)$ in the Wolfeinstein parametrization as shown in Figure 1.1 (b).

1.5 B lifetimes

In the spectator model, a heavy quark (b or c) in a hadron is bound to the lighter "spectator" quark(s). For as long as the spectator holds, the decay is governed by the weak decay of the Q, and, for this reason, the lifetime of all hadrons containing Q are the same and equal to that of a free Q. However lifetimes of B hadrons have been experimentally observed to follow a hierarchy scheme

$$\tau_{B_c} < \tau_{barion} < \tau_{B_s} \leq \tau_{B_d} < \tau_{B_u}. \tag{1.8}$$

On the phenomenological level, the main mechanism generating the observed hierarchy of B hadrons are Pauli interference, Weak annihilation, and Weak Exchange.

1.6 B Mixing

In this section we list the necessary formulas to describe $B^0 - \bar{B}^0$ and $B_s - \bar{B}_s$ mixing. The formulas are general and apply to both B_d^0 and to B_s^0 mesons, although with different values of the parameters. Eqs. (1.9)–(1.21), below are even correct for $K^0 - \bar{K^0}$. $B^0 - \bar{B}^0$ refers to transitions between the two flavor eigenstates $|B^0\rangle$ and $|\bar{B^0}\rangle$. In the Standard Model $B^0 - \bar{B}^0$ is caused by the fourth order flavor-changing weak interaction described by the box diagrams in Fig. 1.2. Such transitions are called $|\delta B = 2|$ transitions, because they change the bottom quantum number by two units. In the Standard Model $|\delta B = 2|$ amplitudes are small, so measurements of $B^0 - \bar{B}^0$ could easily be sensitive to new physics.

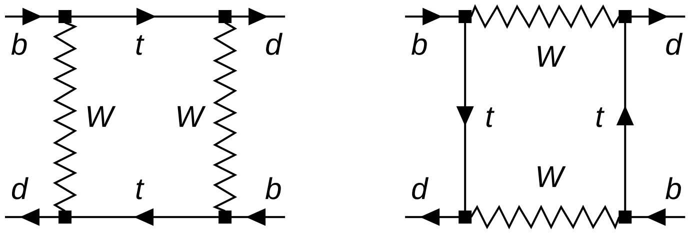

Figure 1.2: Standard Model box diagrams inducing $B_d^0 - \overline{B}_d^0$ mixing.

$B^0 - \bar{B}^0$ induces oscillations between B^0 and $\overline{B}^0$. An initially produced B^0 or $\overline{B}^0$ evolves in time into a superposition of B^0 and $\overline{B}^0$. Let $|B^0(t)\rangle$ denote the state vector of a B meson which is tagged as a B^0 at time $t = 0$, i.e., $|B^0(t=0)\rangle = |B^0\rangle$. Likewise $|\overline{B}^0(t)\rangle$ represents a B meson initially tagged as a $\overline{B}^0$. The time evolution of these states is governed by a Schrödinger equation:

$$i \frac{\mathrm{d}}{\mathrm{d}\,t} \begin{pmatrix} |B(t)\rangle \\ |\overline{B}(t)\rangle \end{pmatrix} = \left(M - i\,\frac{\Gamma}{2}\right) \begin{pmatrix} |B(t)\rangle \\ |\overline{B}(t)\rangle \end{pmatrix} . \tag{1.9}$$

The *mass matrix* M and the *decay matrix* Γ are t-independent, Hermitian 2×2 matrices. CPT invariance implies that

$$M_{11} = M_{22}\,, \qquad\qquad \Gamma_{11} = \Gamma_{22}\,. \tag{1.10}$$

$|\Delta B|\!=\!2$ transitions induce non-zero off-diagonal elements in (1.9), so that the mass eigenstates of the neutral B meson are different from the flavor eigenstates $|B^0\rangle$ and $|\overline{B}^0\rangle$. The mass eigenstates are defined as the eigenvectors of $M - i\,\Gamma/2$. We express them in terms of the flavor eigenstates as

$$\begin{aligned} \text{Lighter eigenstate:} \quad |B_L\rangle &= p|B^0\rangle + q|\overline{B}^0\rangle\,, \\ \text{Heavier eigenstate:} \quad |B_H\rangle &= p|B^0\rangle - q|\overline{B}^0\rangle\,, \end{aligned} \tag{1.11}$$

with $|p|^2 + |q|^2 = 1$. Note that, in general, $|B_L\rangle$ and $|B_H\rangle$ are not orthogonal to each other.

The time evolution of the mass eigenstates is governed by the two eigenvalues $M_H - i\,\Gamma_H/2$

and $M_L - i\,\Gamma_L/2$:

$$|B_{H,L}(t)\rangle = e^{-(iM_{H,L}+\Gamma_{H,L}/2)t}\,|B_{H,L}\rangle\,, \tag{1.12}$$

where $|B_{H,L}\rangle$ (without the time argument) denotes the mass eigenstates at time $t = 0$: $|B_{H,L}\rangle = |B_{H,L}(t=0)\rangle$. We adopt the following definitions for the average mass and width and the mass and width differences of the B meson eigenstates:

$$\begin{aligned} m &= \frac{M_H + M_L}{2} = M_{11}\,, & \Gamma &= \frac{\Gamma_L + \Gamma_H}{2} = \Gamma_{11}\,, \\ \Delta m &= M_H - M_L\,, & \Delta\Gamma &= \Gamma_L - \Gamma_H\,. \end{aligned} \tag{1.13}$$

Δm is positive by definition. Note that the sign convention for $\Delta\Gamma$ is opposite to the one used in Refs. [8, 9, 10, 11]. In our convention the Standard Model prediction for $\Delta\Gamma$ is positive.

We can find the time evolution of $|B(t)\rangle$ and $|\overline{B}(t)\rangle$ as follows. We first invert (1.11) to express $|B^0\rangle$ and $|\overline{B}^0\rangle$ in terms of the mass eigenstates and using their time evolution in (1.12):

$$\begin{aligned} |B^0(t)\rangle &= \frac{1}{2p}\left[e^{-iM_Lt-\Gamma_Lt/2}\,|B_L\rangle \,+\, e^{-iM_Ht-\Gamma_Ht/2}\,|B_H\rangle\right], \\ |\overline{B}^0(t)\rangle &= \frac{1}{2q}\left[e^{-iM_Lt-\Gamma_Lt/2}\,|B_L\rangle \,-\, e^{-iM_Ht-\Gamma_Ht/2}\,|B_H\rangle\right]. \end{aligned} \tag{1.14}$$

These expressions will be very useful in the discussion of B_s mixing.[1] With (1.11) we next eliminate the mass eigenstates in (1.14) in favor of the flavor eigenstates:

$$\begin{aligned} |B^0(t)\rangle &= g_+(t)\,|B^0\rangle + \frac{q}{p}\,g_-(t)\,|\overline{B}^0\rangle\,, \\ |\overline{B}^0(t)\rangle &= \frac{p}{q}\,g_-(t)\,|B^0\rangle + g_+(t)\,|\overline{B}^0\rangle\,, \end{aligned} \tag{1.15}$$

[1] The Schrödinger equation, (1.9), is not exactly valid, but the result of the so-called *Wigner-Weisskopf approximation* [12] to the decay problem. In general, there are tiny corrections to the exponential decay laws in (1.14) at very short and very large times [13]. These corrections are irrelevant for the mixing and CP studies at Run II, but they must be taken into account in high precision searches for CPT violation [14].

where

$$
\begin{aligned}
g_+(t) &= e^{-imt}\, e^{-\Gamma t/2} \left[\quad \cosh \frac{\Delta\Gamma\, t}{4} \cos \frac{\Delta m\, t}{2} - i \sinh \frac{\Delta\Gamma\, t}{4} \sin \frac{\Delta m\, t}{2} \right], \\
g_-(t) &= e^{-imt}\, e^{-\Gamma t/2} \left[-\sinh \frac{\Delta\Gamma\, t}{4} \cos \frac{\Delta m\, t}{2} + i \cosh \frac{\Delta\Gamma\, t}{4} \sin \frac{\Delta m\, t}{2} \right].
\end{aligned} \tag{1.16}
$$

Note that—owing to $\Delta\Gamma \neq 0$—the coefficient $g_+(t)$ has no zeros, and $g_-(t)$ vanishes only at $t = 0$. Hence an initially produced B^0 will never turn into a pure $\overline{B}^0$ or back into a pure B^0. The coefficients in (1.16) will enter the formulae for the decay asymmetries in the combinations

$$
\begin{aligned}
|g_\pm(t)|^2 &= \frac{e^{-\Gamma t}}{2} \left[\cosh \frac{\Delta\Gamma\, t}{2} \pm \cos(\Delta m\, t) \right], \\
g_+^*(t)\, g_-(t) &= \frac{e^{-\Gamma t}}{2} \left[-\sinh \frac{\Delta\Gamma\, t}{2} + i \sin(\Delta m\, t) \right].
\end{aligned} \tag{1.17}
$$

In a given theory, such as the Standard Model, one can calculate the off-diagonal elements M_{12} and Γ_{12} entering (1.9) from $|\Delta B|=2$ diagrams. In order to exploit the formulae (1.14)–(1.16) for the time evolution we still need to express Δm, $\Delta\Gamma$ and q/p in terms of M_{12} and Γ_{12}. By solving for the eigenvalues and eigenvectors of $M - i\,\Gamma/2$ one finds

$$
(\Delta m)^2 - \frac{1}{4} (\Delta\Gamma)^2 = 4\, |M_{12}|^2 - |\Gamma_{12}|^2 \,, \tag{1.18}
$$

$$
\Delta m\, \Delta\Gamma = -4\, \mathrm{Re}\, (M_{12} \Gamma_{12}^*)\,, \tag{1.19}
$$

$$
\frac{q}{p} = -\frac{\Delta m + i\, \Delta\Gamma/2}{2 M_{12} - i\, \Gamma_{12}} = -\frac{2 M_{12}^* - i\, \Gamma_{12}^*}{\Delta m + i\, \Delta\Gamma/2}\,. \tag{1.20}
$$

The relative phase between M_{12} and Γ_{12} appears in many observables related to B mixing. We introduce

$$
\phi = \arg \left(-\frac{M_{12}}{\Gamma_{12}} \right). \tag{1.21}
$$

Now one can solve (1.6) for Δm and $\Delta\Gamma$ in terms of $|M_{12}|$, $|\Gamma_{12}|$ and ϕ.

The general solution is not illuminating, but a simple, approximate solution may be derived when

$$|\Gamma_{12}| \ll |M_{12}| \,, \qquad \text{and} \qquad \Delta\Gamma \ll \Delta m \,. \tag{1.22}$$

These inequalities hold (empirically) for both B^0 systems. We first note that $|\Gamma_{12}| \leq \Gamma$ always, because Γ_{12} stems from the decays into final states common to B^0 and $\overline{B}^0$. For the B_s^0 meson the lower bound on Δm_{B_s} establishes experimentally that $\Gamma_{B_s} \ll \Delta m_{B_s}$. Hence $\Gamma_{12}^s \ll \Delta m_{B_s}$, and Eqs. (1.18) and (1.19) imply $\Delta m_{B_s} \approx 2|M_{12}^s|$ and $|\Delta\Gamma_{B_s}| \leq 2|\Gamma_{12}^s|$, so that (1.22) holds. For the B_d^0 meson the experiments give $\Delta m_{B_d} \approx 0.75\,\Gamma_{B_d}$. The Standard Model predicts $|\Gamma_{12}^d|/\Gamma_{B_d} = \mathcal{O}(1\%)$, but Γ_{12}^d stems solely from CKM-suppressed decay channels (common to B_d^0 and $\overline{B}_d^0$) and could therefore be affected by new physics. New decay channels would, however, also increase Γ_{B_d} and potentially conflict with the precisely measured semileptonic branching ratio. A conservative estimate is $|\Gamma_{12}^d|/\Gamma_{B_d} <$ 10%. Hence for both the B_s^0 and B_d^0 system an expansion in Γ_{12}/M_{12} and $\Delta\Gamma/\Delta m$ is a good approximation, and we easily find

$$\Delta m = 2\,|M_{12}| \left[1 + \mathcal{O}\left(\left|\frac{\Gamma_{12}}{M_{12}}\right|^2\right)\right], \tag{1.23}$$

$$\Delta\Gamma = 2\,|\Gamma_{12}| \cos\phi \left[1 + \mathcal{O}\left(\left|\frac{\Gamma_{12}}{M_{12}}\right|^2\right)\right]. \tag{1.24}$$

We also need an approximate expression for q/p in (1.6). It is convenient to define a small parameter

$$a = \operatorname{Im}\frac{\Gamma_{12}}{M_{12}} = \left|\frac{\Gamma_{12}}{M_{12}}\right| \sin\phi \,, \tag{1.25}$$

because occasionally we need to keep terms of order a. Then q/p becomes

$$\frac{q}{p} = -e^{-i\phi_M}\left[1 - \frac{a}{2}\right] + \mathcal{O}\left(\left|\frac{\Gamma_{12}}{M_{12}}\right|^2\right), \tag{1.26}$$

where ϕ_M is the phase of M_{12},

$$M_{12} = |M_{12}|\, e^{i\phi_M} \,. \tag{1.27}$$

Note that (1.26) and the normalization condition $|p|^2 + |q|^2 = 1$ imply

$$|p| = \frac{1}{\sqrt{2}}\left(1 + \frac{a}{4}\right) + \mathcal{O}\left(\left|\frac{\Gamma_{12}}{M_{12}}\right|^2\right), \qquad |q| = \frac{1}{\sqrt{2}}\left(1 - \frac{a}{4}\right) + \mathcal{O}\left(\left|\frac{\Gamma_{12}}{M_{12}}\right|^2\right). \tag{1.28}$$

1.7 Heavy Quark Effective theory

A very successful theory to describe the decay of the meson containing a heavy and a light quark is the Heavy Quark Effective Theory (HQET), a more detailed treatment is in Ref. [15], where a heavy quark is defined by $m_Q >> \lambda_{QCD}$ with λ_{QCD} $0.2GeV$. In the HQET the Lagrangian is expressed in an expansion in powers of $1/m_Q$, usually referred to as the Operator Product expansion (OPE). In practice only the b and c quarks have masses large enough that HQET is valid. It it does not apply to the top quark because it decays before hadronization.

The lifetime ratio of the B_s/B^0 has been calculated using OPE to be:

$$\frac{B_s}{B^0} = 1 \pm 0.01 \tag{1.29}$$

In conclusion lifetime ratios are predicted by theory very precisely hence they can give us a powerful tool to test the Standard Mode. This is possible only if we can measure such lifetimes an ratios beyond the error in the theoretical prediction, such a task it is feasible in the new generation of detectors, and in particular in the DØ experiment. That is the main reason for this analysis. Our goal was reached with satisfaction, in the way we have learned some aspects of the lifetime phenomena unknown until now. Also this work is the basis for a more advance analysis consisting in separate the two CP eigenstates in the B_s with hints of new physics.

The organization of the present thesis is as follows in Chapter 1 we presented a theoretical introduction consisting in a brief description of the standard model, the CKM matrix , and some description of CP violation, mixing, and the Heavy quark expansion used for lifetimes ratio prediction. In the next Chapter we describe the detector and some generalities of the reconstruction and the framework used. In Chapter 3 we describe the method to calculate the lifetime and the cuts to extract the signal, we also examine the cross feed contamination. In the Chapter 4 we give the PDF used for the fit of the lifetime. In the following Chapter we show the fitting results. Finally we show the results and future prospect of this dissertation.

Chapter 2

Detector Description

2.1 Tevatron

The Tevatron is a $p\bar{p}$ collider that accelerates protons and antiprotons to an energy of 980 GeV, providing a center of mass energy of 1.96 TeV. A schematic view is in Figure 2.1.

The proton beam originates from the preaccelerator, where negatively charged hydrogen ions are accelerated to 750 keV in a Cockroft-Walton accelerator. From there, the hydrogen ions are bunched and led into a 150 meter long linear accelerator (LINAC), which accelerates the hydrogen ions to an energy of 400 MeV, after which they are fed into a circular accelerator, calls the booster. Here, the ions are led through a carbon foil which strip both electrons from the hydrogen nucleus, leaving the proton. The proton are then accelerated to an energy of 8 GeV. After this stage, they enter the main injector. This circular accelerator serves with two purposes: it separately accelerates proton and antiproton from 8 GeV to 150 GeV for subsequent insertion in the Tevatron, and protons are accelerated from 8 GeV to 120 GeV for the production of anti protons. The anti-protons are produced by colliding the proton that have been accelerated in the main injector to an energy of 120 GeV on a nickel target. These collisions produce many secondary particles, among which are antiprotons, approximately one for every 10^5 protons. The antiprotons produced are temporally stored in a circular ring, called the accumulator. When approximately 10^{11} antiprotons have been produced, they are assembled, bunched and inserted in the main injector to an energy of 150 GeV for injection in the Tevatron. The tunnel of the main injector also holds the antiproton recycler, which stores decelerated antiprotons coming from the previous run in the Tevatron for future use. After separate acceleration of the protons and antiprotons in the main injector to an energy of 150 GeV, both beams are inserted in the Tevatron, where they are further accelerated to an energy of 980 GeV.

The Tevatron uses superconducting magnets with a filed strength of 4.2 Tesla (at a beam energy of 980 GeV) to bend the protons and antiprotons through the 1000-meter radius tunnel. The proton beam traverses the Tevatron clockwise, while the antiproton beam moves in the opposite direction. The beams meet at the two interactions points, at the BØ, where the CDF detector is located, and at the DØ, where the DØ detector is located.

Some parameters have changed for RunII significantly from the Run I. Some parameter are given in table 2.1

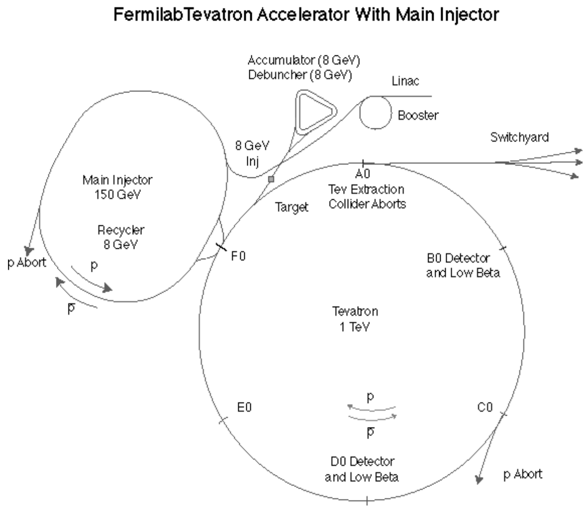

Figure 2.1: A Tevatron scheme. Not to scale.

Parameter	value
maximum beam energy (TeV)	0.980
Luminosity ($10^{30} cm^{-2} s^{-1}$)	50
Time between collision (μs)	0.396
Crossing angle (μrad)	0
Energy spread (units 10^{-3})	0.14
Bunch length(cm)	57
Beam radius (10^{-6} m)	p:39 ,$\bar{p}$:31
Free space at interaction point (m)	± 6.5
Luminosity lifetime(hr)	11-13
Filling time (min)	30
Acceleration period(s)	86
Particles per bunch (units 10^{10})	p:24, $\bar{p}$: 3
Bunches per ring per species	36
Magnetic length dipole (m)	6.12
Circumference (km)	6.28
Dipoles in ring	774
Quadrupoles in ring	216
Peak magnetic field(T)	4.4

Table 2.1: Tevatron Parameters

2.2 Introduction

The DØ experiment was proposed in 1983 to study proton-antiproton collisions at $\sqrt{s} = 1.8$ TeV at the Fermilab collider. The focus of the experiment was the study of high mass states and large p_T. The detector performed very well during Run I of the Tevatron, 1992-1996, leading to the discovery of the Top Quark [16], and measurement of its mass [17] [21], among many other accomplishments [23].

In Run II, the tevatron is operated with 36 bunches of protons an antiprotons with a bunch spacing of 396 ns, and a center-of-mass energy of 1.96 TeV. The instantaneous luminosity will be greater than $10^{32} cm^{-2} s^{-1}$ and more than 4 fb^{-1} of data is expected to be recorded. To take advantages of the improvements in the Tevatron and to enhance the physics reach of the experiment, we have significantly upgraded the DØ detector.

The detector consist of three major subsystems: central tracking detectors, uranium/liquid-argon calorimeters, and a muon spectrometer. The original DØ Detector is described in de-

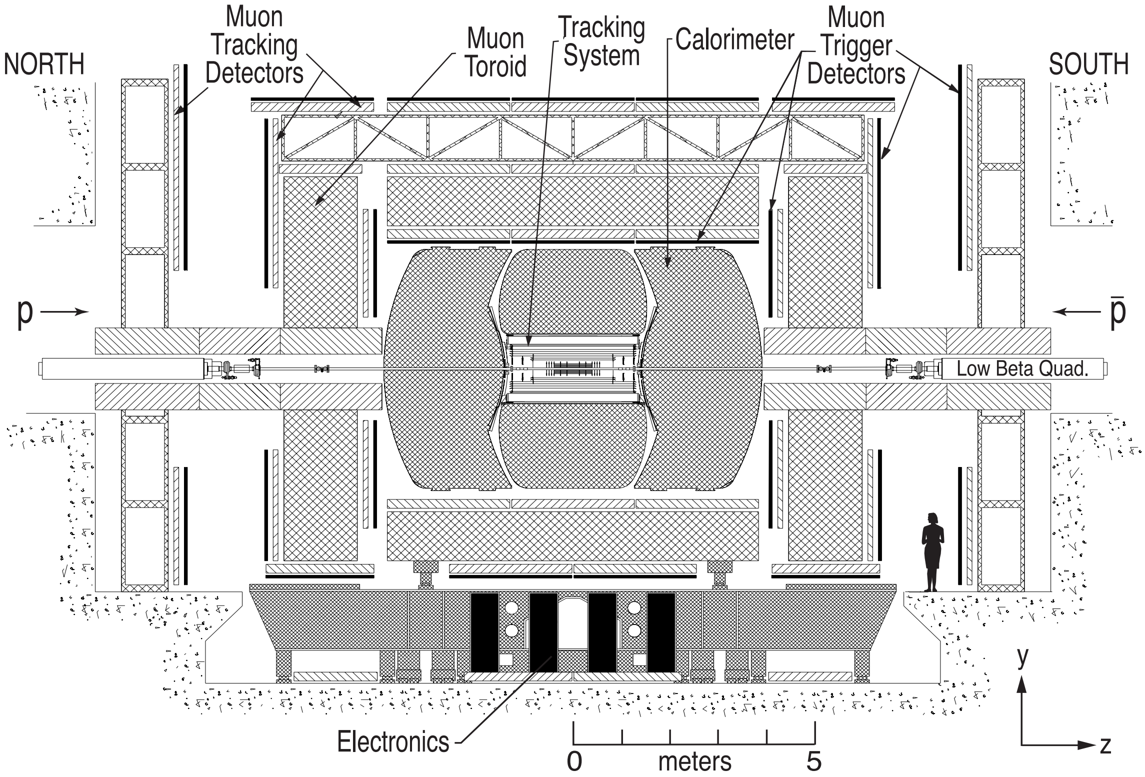

Figure 2.2: Diagram of the upgraded DØ detector, as installed in the collision hall and viewed from inside Tevatron ring. The $+z$ axis is to the right, $+y$ is up, and $+x$ is out of page.

tail in Ref.[24]. The new system includes a silicon microstrip tracker and a scintillator-fiber tracker located within a 2 T solenoidal magnet. The silicon microstrip tracker is able to identify displaced vertex for b-quark tagging, and also measuring of mesons lifetimes. The Forward muon system's proportional drifts chambers have been replaced by minidrift tubes and trigger scintillation counters that can withstand the harsh radiation environment and additional shielding has been added. In the central region, scintillation counters have been added for improved muon triggering. A side view of the upgraded DØ detector is show in Figure 2.2.

In detector description and data analysis, we use a right-handed coordinate system in which the z-axis is along the proton direction an the y-axis is upward (Figure 2.2). The angles ϕ and θ are the azimuthal and polar angles, respectively, the r coordinate denotes the perpendicular distance form z axis. The pseudo-rapidity, $\eta = -ln[tan(\theta/2)]$, approximates

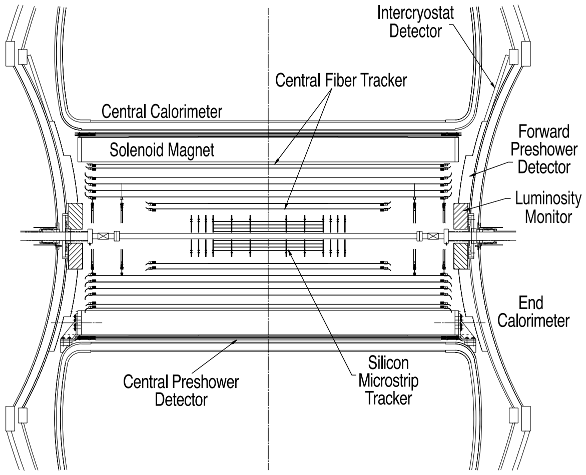

Figure 2.3: The new central tracking system. Also shown are the locations of the solenoid, the preshower detectors, luminosity monitor, and calorimeters. Not to scale.

the true rapidity, $y = 1/2 \ln[(E+p_z c)/(E-p_z c)]$, for finite angles in the limit $(mc^2)/E \to 0$. We use the term "Forward" to describe the regions at large" $|\eta|$.

In the following section we will give a description of the components of the detector, focusing in the relevant components to this analysis, for completeness we will mention all components of the detector.

2.3 Central tracking

The central tracking system consist of the silicon microstrip tracker (SMT) and the central fiber tracker (CFT) surrounded by a solenoidal magnet. Working together, the two detectors locate the primary interaction vertex with a resolution of about 35 μm along the beamline. A schematic view of the central tracking system is shown in Figure 2.3

2.3.1 Silicon microstrip tracker

The SMT provides both tracking and vertexing over nearly the full η coverage of the calorimeter an muon system. The length of the interaction region ($\sigma \approx 25$ cm) sets the length scale of the device. With a long interaction region, it is difficult to deploy detectors such that the tracks are generally perpendicular to detector surfaces for all η. This led us to a design of barrel modules interspersed with disk in the center and assemblies of disk in the forward regions. The barrel detectors primarily measure r-ϕ coordinate an the disk detector measure r-z as well as r-phi. Thus vertexes for high η particles are constructed in three dimensions by the disks, and vertexes of particles at small values η are measured in the barrels and central fiber tracker.

An isometric view of the SMT is shown in Figure 2.4. The detector has six barrels in the central region. Each barrel has four silicon readout layers. The silicon modules installed in the barrels are called "ladders" . Layers 1 and 2 have twelve ladders each. Layers 3 and 4 have twenty-four ladders each, 72 ladder per barrel for a total of 432 ladders. Each barrel is capped at high $|z|$ with a disk of twelve double sided wedge detectors, called an "F-disk" . Forward of each disk/barrel assembly is a unit consisting of three "F-disks". In the far forward regions, two large-diameter disks , "H-disks" provide tracking at high $|\eta|$. Twenty-four full wedges, each consisting of two back-to-back single-sided "half" wedges, are mounted on each H-disk. There are 144 F-wedges and 96 full H-wedges in the tracker; each side of a wedge (upstream and downstream) is read out independently. There is a grand total of 912 readout modules , with 792,576 channels. The centers of the H-disks are located at $|z| = 100.4$, 121.0 cm; the F-disks are at $|z| = 12.5$, 38.2, 43.1,48.1, and 53.1 cm.

The detector uses a combination of single sided (SS), double sided (DS), and double-sided double-metal (DSDM) technology. All sensors were required to exhibit a leakage current less than $260nA/cm^2$ and each channel was tested for leakage current, AC coupling capacitance, and AC coupling leakage to 80 V. A set of radiation damage qualification studies with the results that microdischarge in the DSDM detectors will limit the lifetime of the SMT to a integrated luminosity of $3.5 - 6fb^{-1}$. Barrel ladders are supported by beryllium bulkheads machined with the posts and pinholes for ladder support. Disks are supported by beryllium rings.

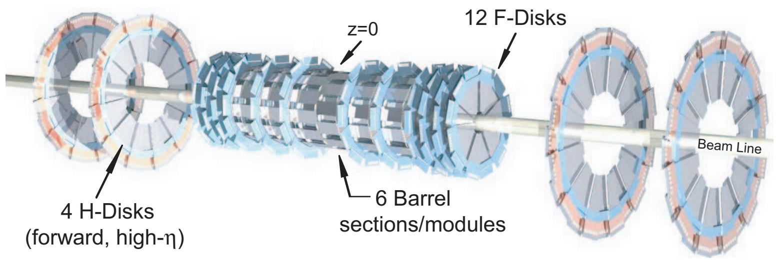

Figure 2.4: The disk/barrel design of the silicon microstrip tracker (SMT),

2.3.2 Central fiber tracking

The CFT consist of scintillating fibers mounted on eight concentric support cylinders and occupies the radial space from 20 to 52 cm from the center of the beampipe. The two innermost cylinder are 1.66 m long; the outer six cylinders are 2.52 m long. Each cylinder supports one doublet layer of fibers oriented along the beam direction (z) and a second doublet layer at stereo angle of $+3^o(u)$ or $-3^o(v)$. Doublet layers with fibers oriented along the beam axis are referred to as axial layers, while the doublet layers oriented at small angles to as stereo layers. From the smallest cylinder outward , the fiber orientation is $zu-zv-zu-zv-zu-zv-zu-zv$. The scintillator fibers are coupled to clear fiber waveguides which carry the scintillation light to visible photon counters (VLPCs) for readout. The small fiber diameter gives fiber of the CFT an inherent doublet layer resolution of about 100 μm.

Signal form the axial doublet layers are used to form a fast Level 1 hardware trigger based upon the number of track candidates above a specific p_T threshold (with a minimum threshold of 1.5 GeV/c). Level 1 track candidates are used for the Level 2 trigger, and the Level 3 trigger uses the full CFT readout.

The scintillating fibers, including cladding, are 835 μm in diameter and 1.66 or 2.53 m in length. They are optically connected to clear fibers waveguides of identical diameter which are 7.8 to 11.9 m long. The fibers have a multi-clad structure consisting of a core surrounded by two claddings. The scintillating fiber is structurally and chemically similar to the clear fiber, but contains fluorescent dyes. The CFT uses about 200 km of scintillating fiber and 800 km of clear fiber.

Light production in the fibers is a multistep process. The bass core material is polystyrene (PS). The PS is doped with the organic fluorescent dye paraterphenyl(pT) to about 1% in weight. Excitations in the PS are rapidly transferred to the pT via a non-radiative dipole-dipole interactions. pT has a rapid florescence decay (a few nanoseconds) and a short emission wavelength (approx. 340 nm). The mean free path of the emitted light is only a few hundred microns in the PS. To get the light out of the detector, a secondary or wave shifter, dye, 3-hydroxyflavone (3HF), is added at low concentration (1500ppm). The 3HF is spectrally matched to the pT but has a minimal optical self-absorption. The 3HF absorbs the 340 nm radiation from the pT and re-emits it at 530 nm which is well transmitted in PS.

Surrounding the PS core, whose refractive index is $n = 1.59$, are two claddings, each approximately 25 μm thick: an inner layer of polymethylmethacrylate (PMMMA) with n= 1.49, and a outer layer fluoro-acrylic with n=1.42, the PMMA inner cladding serves as a mechanical interface between the core and the outer cladding, which are mechanically incompatible. The multiclad fibers is both mechanically an optically superior to single-clad fiber and typical values of the attenuation length are about 5 m for the scintillator fibers and 8 m for the clear fiber.

We observe light form only one end of each scintillator fiber. The opposite end of each of the scintillator fibers was mirrored by sputtering with an aluminum coating that provides a reflectivity of 85% to 90%.

The scintillators fibers were made into ribbons consisting of 256 fibers in two layers of 128 fibers each. Precisely spaced grooves were machined into a long, 1/16”-thick piece of Delrin plastic. The spacing between groves varies between 928 and 993 μm and depends on the radius of the corresponding support cylinder. The grooved plastic was inserted into a rigid, curved backing with the desired radius and the scintillator fibers were laid in and glued together to form the doublet ribbons; the two layers of fiber are offset by one-half of the fiber spacing. The technique is illustrated in Figure 2.5 and creates curved ribbons to match the curvature of each support cylinder without machining precisely spaced grooves into a curved surface.

The readout ends of the fibers were carefully positioned and adhesively bonded into v-groove connectors, and the mass-terminated ribbon and connectors were polished to facilitate high efficiency light transmission across the connectors. The light transmission through the v-groove connectors, with optical grease between the fibers ends, is approximately 95

The position of each fiber within the ribbon was verified with and accuracy of better than 25 μm rms.

The eighth mechanical support for the CFT consist of eight carbon fibers support cylinders double walled with a 0.25"-thick core of Rohacell. For tracks traversing the detector at normal incidence, the thickness of each cylinder can be broken down as follows: 0.28% of radiation length fo the scintillators fibers, 0.32% for the carbon fibers support cylinder, 0.13% for the glue used to make the ribbons out of fibers, and 0.17% for the glue used to attach the ribbons to the support cylinders.

The light generated by the passage of charged particles through the scintillator fibers of the CFT is converted into electrical signal by the VLPCs, housed in the VLPC cassettes. VLPCs are impurity-band silicon avalanche photodetectors that operate at 9K, an are capable of detecting single photons. They provide fast response, excellent quantum efficiency ($>$ 75%) high gain (17,000 to 65,000) , low gain dispersion, and capability of functioning in a high background environment.

The CFT requires 76,800 channels of VLPC readout. Better than 99.8% of the individual VLPC channels in these cassettes met or exceeded the desired performance specification during cryogenic qualifications test preformed prior to installation at DØ

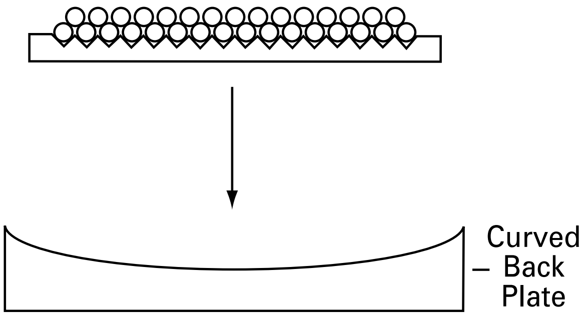

Figure 2.5: Technique for curved scintillating fiber ribbon fabrication.

2.4 Solenoidal Magnet

The superconducting solenoidal magnet was designed to optimize the momentum resolution, $\delta p_T/p_T$, and tracking pattern recognition within the constraints imposed by the Run I detector. The overall physical size of the magnet was determined by the space available within the central calorimeter vessel: 2.73 m in length and 1.42 m in diameter. We selected a central field of 2 T after considering the momentum resolution and tracking pattern recognition, the available space, and thickness of the cryostat which depends on the thickness of the conductor and support cylinder. Services such as cryogens, magnet high currents buses, and vacuum pumpout and relief must reach the magnet from the control dewar; that is the interface between the fixed cryogenic piping and the movable detector through the narrow space (7.6 cm) between the central and end calorimeter vacuum vessels. The magnet system is controlled remotely, including cool down, energization, de-energization for field reversal, quench recovery and warmup, without access to the magnet cryostat, service chimney , or control dewar.

A perspective view of the solenoid inside the central calorimeter with its chimney and control dewar is shown in Figure 2.6.

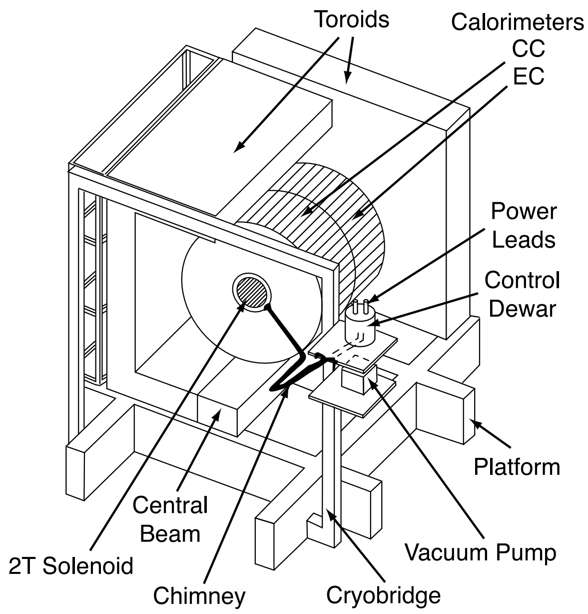

Figure 2.6: Perspective view of the solenoid inside the central calorimeter. One end calorimeter and several muon chambers have been omitted for clarity. Also shown are the service chimney and the control dewar.

2.4.1 Magnetic field

The magnetic field of the full magnet system is modeled using the TOSCA [22] program. The calculated field map was compared with the measured filed in two locations: near the internal radius of the solenoid cryostat ($r \approx 54cm$) at z = 4 an in the gap at the top of the central muon toroid steel. Within the solenoid the measured filed is 20.141 ± 0.005 kG; the calculated field at this location is 20.158 kG. The calculated magnetic field is scaled by 0.09% to agree with the measurement. With full operating current in the toroid coils here is a 4.5% difference between the calculated and measured field at the CF gap, requiring an adjustment in the calculated field for the CF toroid. A $y - z$ view of the magnetic field with both the toroid and solenoid magnets at full current is show in figure 2.7

2.5 Preshower Detectors

The preshower detector aid in the electron identification and background rejection, They function as calorimeter as well as tracking detectors, enhancing the spacial matching between tracks and calorimeter showers. The central preshowers detectors (CPS) covers the regions

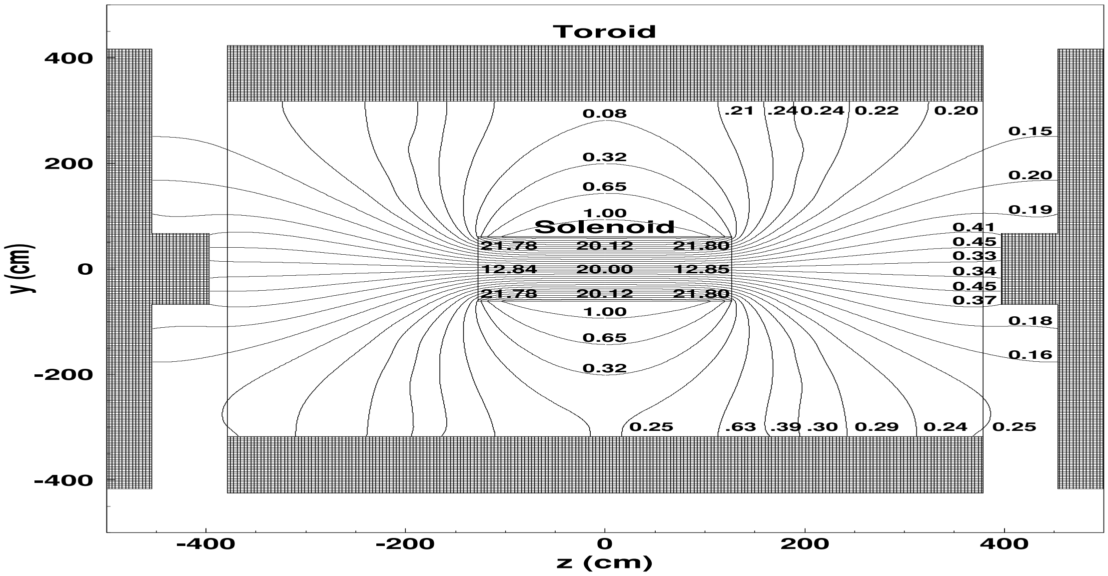

Figure 2.7: The $y - z$ view of the DØ magnetic field with both the toroid and solenoid magnets at full current. The field lines are projections onto the $y - z$ plane; the left and right line ends differ by up to 2.5 m in x. The numbers give strength of the magnetic filed at various locations in kG.

$|\eta| < 1.3$ and is located between the solenoid an the central colorimeter. The two forward preshower detectors (FPS) cover $1.5 < |\eta| < 2.5$ and are attached to the faces of the end of the calorimeters. The locations of the preshower are shown in Figure 2.3. Since in this analysis we do not use the preshowers because of that we will not give further description. For a more complete description use Ref. [27].

2.6 Calorimeters

The DØ calorimeter consist of three uranium/liquid argon calorimeter and the intercryostat detector. The calorimeter were designed to provide the energy measurement for electrons, photons, and jets in the absence of a central magnetic field (as was the case during Run I on the Tevatron) , as well as assist in the identification of electrons, photons, jets and muons and establish the transverse energy balance in an event. The calorimeter themselves are unchanged from Run I and are described in detail in Ref. [24]. They are shown in Figure 2.2.

The Central calorimeter (CC) cover $|\eta| \leq 1$ and the two end calorimeters, ECN (north) and ECS (south), extend coverage to $|\eta| \approx 4$. Each calorimeter contains an electromagnetic section closest to the interaction region followed by fine and coarse hadronic sections. The active medium for all of the calorimeters is argon and each of the three calorimeters (CC,ECN,ECS) is located within a cryostat that maintains the temperature at approximately 80 K. Different absorber plates are used in different locations. The electromagnetic sections (EM) use thin (3 or 4 mm in the CC and EC, respectively) plates, made from nearly pure depleted uranium. The fine hadronic sections are made from 6-mm-thick uranium-niobium (2%) alloy. The coarsic hadronic modules contains a relatively thick (46.5 mm) plates of either cooper in the CC or stainless steel in the EC. Since this detector play a very modest role in the analysis we will not describe more of it, see Ref. [27] for a more detailed description.

2.7 Muon system

Muons played a main part in the analysis of B_s and B_d since two of the four final particles are muons, and even more we use the $J/\psi \to \mu^+\mu^-$ as our very first discriminating criteria.

For Muon triggering and measurement, the upgraded detector uses the original central muon system proportional drift tubes (PDTs) and toroidal magnets, central scintillator counters (some new and some installed during Run I), and a completely new forward muon system. The central muon system provides coverage for $|\eta| \leq 1.0$. The new forward muon system extends muon detection to $|\eta| \approx 2.0$, uses minidrift tubes (MDTs) rather that PDTs, and includes trigger scintillator counters and beam pipe shielding.

During Run I, a set of scintillators counters, the cosmic cap , was installed on the top and upper sides of the outer layer of the central muon PDTs. This coverage has been extended to the lower sides and bottom detector, to form the cosmic bottom. These trigger scintillator counters are fast enough to allows us to associate a muon in a PDT with the appropriate bunch crossing and to reduce the cosmic ray background. Additional scintillator counters,

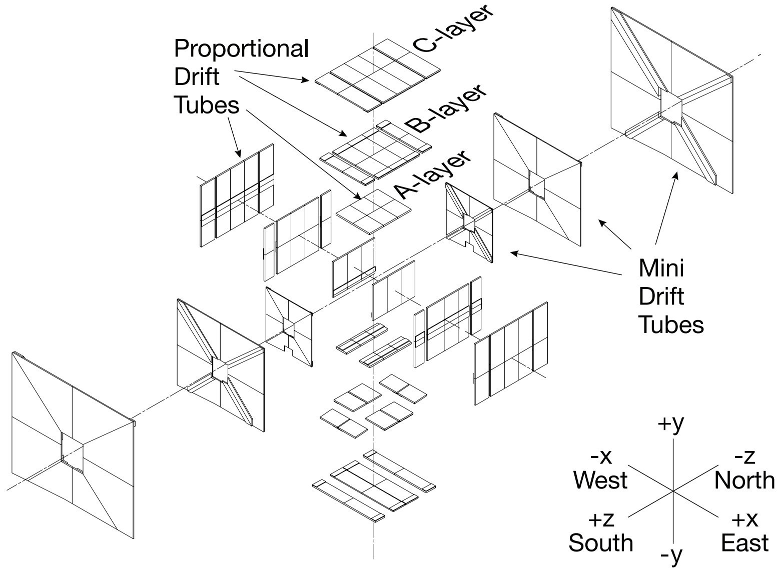

Figure 2.8: Exploded view of the muon wire chambers.

the Aϕ counters, have been installed on the PDTs mounted between the calorimeter and the toroidal magnet. The Aϕ counters provide a fast detector triggering and identifying muons for rejecting out-of-time background events.

The scintillators counters are used for triggering; the wire chambers are used to precise coordinate measurements as well as triggering. Both types of detectors contribute to background rejection: the scintillator with timing information an the wire chambers with track segments. Exploded views of the muon system are shown in Figures 2.8 and 2.9.

2.7.1 Toroidal magnets

The Toroidal magnets are described in detail in Ref. [24] and shown in Figure 2.2. Having a Stand-alone muon-system momentum measurement: enables a low p_T cutoff in the Level1 muon trigger, allow for a cleaner matching with the central detector tracks, rejects π/K decays and improves the momentum resolution for high momentum muons.

The central toroid is a square annulus 109 cm thick whose inner surface is about 318 cm from the Tevatron beamline; it covers the region $|\eta| \leq 1$. The two ends toroids are located at $454 \leq |z| \leq 610$cm. In the center of each toroid is a 183 cm square hole centered on the beamline. In x and y the magnets extends 426 cm from the beamline. During Run II, the magnets are being operated at series, at a current of 1500A. As in Run I, the polarity of the magnets during data collection is regularly reversed.

2.7.2 Central muon detector

The central muon system consist of a toroidal magnet, drift chambers, the cosmic cap an a bottom scintillation counters, an the Aϕ scintillation counters.

2.7.3 Central muon drift chambers

The central drift chambers consist in three layers of drift chambers: one inside the toroidal magnet called A-layer and two outside called B-layer and C-layer, and cover $|\eta| \leq 1$. Approximately 55% of the central region is covered by three layers of PDT; close to 90% is covered by at least two layers. The drift chambers are large, typically 2.8 X 5.6 m^2, and made of rectangular extruded aluminum tubes. The PDTs outside the magnets have three decks of drift cells; the A-layer has fourth decks with the exception of the bottom A-layer which have three decks. The cells are 10.1 cm across; each chamber is 24 cells wide an typically contains 72 or 96 cells. Along with anode wire at the center of each cells, vernier cathode pads are located above an below the wires to provide information on the hit position along the wire. the wire are ganged together in pairs within a deck an then read by electronics located at the end of each chamber.

For each PDT hit the following information is recorded: the electron drift time, the difference ΔT in the arrival time of the hit between a hit cell an the neighbor connected to it, and the charge deposition on the inner an outer vernier pads. Both ΔT and the charge deposition are used to determine the hit position along the wire. The drift distance resolution is $\sigma \approx 1mm$. The resolution of the ΔT varies from 10cm to 50 cm. Using charge division the pad signal resolution is about 5mm.

To reduce the number of bunch crossing which occur during one maximum drift time interval, we are using a faster gas mixture than we used during Run I. The new mixture is 84 % argon, 8 % methane, and 8 %CF_4. The operating high voltage is 2.3 kV for the pads and 4.7 kV for the wires. The drift velocity is approximately 10 $cm/\mu s$, for a maximum drift time of about 500 ns. The contribution to the hit position uncertainty due to diffusion is about 0.4 mm.

2.7.4 Cosmic cap and bottom counters

The cosmic cap for bottom counters are installed on the top, sides and bottom of the layer of the central muon PDTs. They provide a fast timing signal to associate a muon in a PDT with the appropriate bunch crossing and discriminate against the cosmic ray background.

The cosmic cap counters are made from grooved 0.5” Bicron 404a scintillator with BCF 91 and a Kuraray Y11 wave-shifting fibers glued into the groves using bicron 600 optical epoxy. there are 240 counters, 25” wide, and 81.5”-113” long. The counters are positioned with their width along z and length along ϕ . The grooves are 1.75 mm deep and 4 mm wide; they run along the length of the counter, from end to just pass the center of the counter. They are spaced 8 mm apart so that half of the surface is covered with fibers. Each groove contain four fibers. The fibers are read using phototubes.

The cosmic bottom complete the scintillator coverage of the central toroidal magnet. There are 132 counters of two different design. The forty eight counters located in the outside of the center of the bottom layer B-layer of PDT, are nearly identical to the cosmic cap counters described above. The sixty-eight counters located on the undersides of the remaining B and C layers are similar to the cosmic cap counters except that the bottom counters have fewer fibers and are placed in vertical, rather than horizontal, grooves.

An important difference between the cosmic cap and the cosmic bottom counters is that the bottom counters are positioned with their narrow dimension along ϕ an their long dimension along η. This orientation has better matching in ϕ with the central fiber tracker trigger.

2.7.5 Aϕ scintillator counters

The Aϕ scintillator cover the A-Layer PDTs, those between the calorimeter and the toroid. They provide a fast detector for triggering on and identifying muons and for rejecting out-of-time backscatter from the forward direction. In-time scintillation counter hits are matched with tracks in the CFT level 1 trigger for high-p_T single muon and for low-p_T dimuon triggers. The counters also provide the time stamp for low-p_T muons which did not penetrate the toroid and thus do not reach the cosmic cap or bottom counters.

The layout of the forward muon system is shown in Figure 2.2. It covers $1.0 \leq |\eta| \leq 2.0$ and consist of four major parts: the end toroidal magnet, three layer of MDTs for muon track reconstruction, three layer of scintillator counters for triggering on events with muons, and shielding around the beam pipe.

Mini drift tubes were chosen for their short electron drift time (less that 132 ns), good coordinate resolution (less than 1 mm), radiation hardness, high segmentation, and low occupancy, The MDTs are arranged in three layers (A, B, and C, with A closest to the interaction region inside the toroidal magnet and C furthest away), each of which is divided into eight octant's Figure 2.8. A layer consist of three (layers B and C) or four (layer A) planes of tubes; each tube comprises eight $1 \times 1 cm^2$ cells. The tubes are mounted along magnetic field lines (the field shape in the forward toroids is more "square" than "circular"). The entire MDT system contains 48,640 wires; the maximum tube length is 5830 mm in layer C.

The efficiency of the MDT is 100% in the active area of the cells for tracks which are perpendicular to the MDT plane. The overall plane efficiency is less, due to the wall thickness and PVC sleeves, and is approximately 95% for our geometry.

The momentum resolution of the forward muon spectrometer is limited by multiple scattering in the toroid and the coordinate resolution of the tracking detector. The standalone momentum resolution of the forward muon system is approximately 20% for muon momentum below 40 GeV/c. The overall muon momentum resolution, including information from the SMT and CFT, is defined by the central tracking system for muons with momentum up

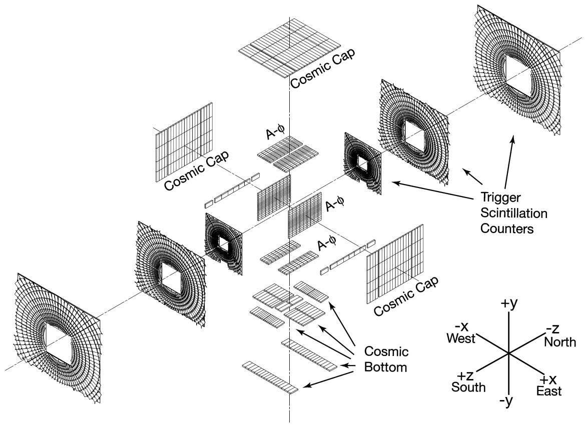

Figure 2.9: Exploded view of the muon scintillation detectors. Note that the backs of the scintillation detectors are shown for the south end.

to approximately 100 GeV/c; the forward muon system improves the resolution for higher momentum muons and is particularly important for tracks with $1.6 \leq \eta \leq 2.0$, i.e. those which do not go through all layers of the CFT.

2.7.6 Trigger scintillation counters

The muon trigger scintillator counters are mounted inside (layer A) or outside (layer B and C) of the toroidal magnet (Figure 2.2). Each layer is divided into octants containing about ninety-six counters. The ϕ segmentation is 4.5^o and matches the CFT trigger sectors. The $\eta = 0.12(0.07)$ for the first inner (last three) rows of counters. The largest counters, outers counters in the C layer, are $60 \times 110cm^2$. The B and C layers have geometries similar to that of the A layer, but limited in places by the collision hall ceiling and floor.

2.8 Forward proton Detector

There is a forward proton detector that measures protons and antiproton scattered at small angles (of the orders of 1 mrad) that are missed by the main DØ detector. These detector is not used in this analysis. And we will not talk further on it.

2.9 Luminosity monitor

The primary purpose of the luminosity monitor (LM) is to make an accurate determination of the Tevatron luminosity at the DØ interaction region. This is accomplished by detecting inelastic $p\bar{p}$ collisions in a dedicated detector. The LM also serves to measure the beam halo rates, to make a fast measurement of the z-coordinate of the interaction vertex, and to identify beam crossings with multiple $p\bar{p}$ interactions. In these analysis we did not use a specific trigger. The luminosity estimation was done in an approximate way we will explain the method in the analysis section.

2.10 Triggering

As explained above we did not use a specific trigger. The trigger system in DØ consist of three levels. The first stage (Level 1 or L1) comprises a collection of hardware trigger elements that provide a trigger accept rate of 1.6 kH. In the second stage (Level 2 or L2), hardware engines and embedded microprocessors associated with specific subdetectors process information used by a global processor in determining correlations between different detectors. L2 decisions are made within $100\mu s$ with an accept rate of about 1 kHz. Candidates from L1/L2 are passed to a farm of level 3 (L3) microprocessors sophisticated algorithms reduce the rate to about 50 Hz and these events are recorded for offline reconstruction. A block diagram of elements of the DØ trigger system is shown in Figure 2.10.

2.11 Event Simulation

The DØ event data model (EDM) is a library of C++ classes and templates whose purpose is to support the implementation of reconstruction and analysis software.

The conversion of the C++ objects used in the reconstruction program to a persistent format is handled by the DØ object model (DOoM) [28]. First, DOoM maintains a dictionary describing the layout of the C++ classes that are used persistently, which is generated by

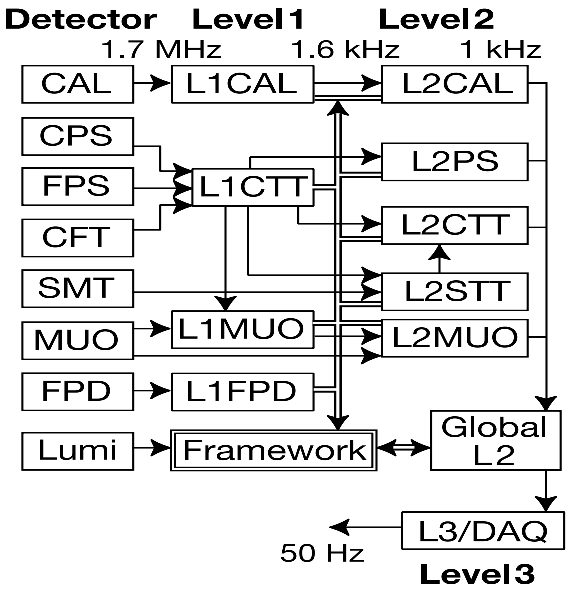

running a preprocessor over the C++ headers defining the classes. This preprocessor is based in a modified version of the CINT C/C++ interpreter (which also is used in the ROOT system [29]).

The generation of Monte Carlo (MC) events involves multiple stages and many executables. To integrate all processes, all programs use the EDM to carry data in memory and DOoM to store persistent data. All code is organized in independent packages running in a standard DØ framework and is written in C++ or embedded in C++ driving routines.

The first step in MC event generation is the simulation of a physical process, a $p\bar{p}$ collision producing a particular final state. Nearly all existing event generator programs are written in Fortran, but the StdHep [30] code from FNAL Computing Division can be used to store the output is a standard common block format. This allowed us to write a C++ wrapper that converts the StdHep Fortran format to C++ classes satisfying the EDM requirements.

To trace particles through the DØ detector and to determine where their paths intersect active areas, and to simulate their energy deposition and secondary interactions, we use the CERN program GEANT v3.21 [31], which also is written in Fortran. A C++ wrapper is used to read files produced by the event generators and write the output of GEANT in DOom format. this executable is called DØGSTAR. All subsequent steps in the event simulation are handled by programs written almost entirely in C++.

The DØSIM program modifies the generated Monte Carlo data to account for various detector-related effects. After particles from the simulated reaction have been traced through the detector, the generated energy depositions must be converted to the form that the real data takes when processed through the DØ electronics. Detector inefficiencies and noise (from detector and electronic readout) must be taken into account, and more than one interaction may occur during beam crossing. In addition, some portions of the detector (such as the calorimeter) remain sensitive to interactions over the period of time that includes more than one beam crossing. Simulation of the trigger electronics and the effects of trigger on data selection is performed by a separate program, DØTRIGSIM. DØTRIGSIM contains simulation code only for the L1 trigger. The L2 and L3 triggers are based on filtering code, and exactly the same software run in DØTRIGSIM. The output of the DØSIM and DØTRIGSIM is in the same format as the data recorded at DØ data acquisition system, but contains additional MC information to make it possible to correlate detector data with the original generator output.

2.12 Reconstruction

The DØ offline reconstruction program (RECO) is responsible for reconstructing objects used from physics analysis. It is a CPU-intensive program that processes collider events recorded during online data taking and simulated MC events. The executable is run on the offline farms and the results are placed into the central data storage system for further analysis. Information and results for each event are organized using the EDM. The EDM manages information within the event blocks called chunks. The raw data chunk (RDC), created either by an L3 processor node or the MC, contains the raw detector signals and is the primary input to RECO. The output from RECO consist of many additional chunks associated associated with each type of reconstructed object. RECO produces two formats or data tiers. The data summary tier (DST) contains all information necessary to perform any physics analysis, including limited re-reconstruction of high-level physics objects. The thumbnail (TMB) is a physics summary format less than one-tenth the size of the DST format. the TMB can be used directly to perform many analysis, and it allows the rapid development of event selection criteria to be applied to the DST sample.

RECO reconstruct events in several hierarchical steps. The first involves detector-specific processing. Detector unpackers process individual detector data blocks within the RDC, decoding the raw data information, associating electronic channels with physical detector elements, and applying detector-specific constants. For many of the detectors , this information is then used to reconstruct a cluster (for example, from the calorimeter and preshower detectors) or hit (from racking detectors) objects. These objects use the geometry constants to associate detector elements (energies and positions) with physical position in space. The second step in RECO focuses on the output of the tracking detector, reconstructing global tracks from hits in the SMT and CFT. This process, involving several different tracking algorithms is the most CPU-intensive activity or RECO. The results are stored in corresponding tracks chunks, which are used as input to the third step in RECO vertexing. First primary vertex candidates are found . These vertexes indicate the location of the $p\bar{p}$ interactions and are used in the calculation of various kinematic quantities (e.g. E_T). Next, displaced vertex candidates are identified. Such vertexes are associated with decays of long-lived particles. The results of the above algorithms, information from each of the preceding reconstruction steps in combined and standard physics objects candidates are created. RECO first find electron, photon, muon neutrino ($/E_T$), and jet candidates, after which it identifies candidates for heavy-quark. Tau are identified next.

Chapter 3

Cuts and cross feed contamination

In the following lines we will describe the method used to calculate the lifetime of the B_s and B_d mesons. first we will describe the selection of the data since we have million of events to analyze. this is actually one of the toughest and more labor consuming part of the analysis,and we will try to be as explicit as we can. Next we will make a Monte Carlo analysis of a possible cross feed contamination between B_s and B_d mesons.

3.1 Data selection

3.1.1 Global cuts

A cut is a selection criteria we use to eliminate the events that are not interesting for us. For example, if in a given event we do not have a primary vertex, how can we measure the decay distance?. A global cut is a cut that we decide not to use in the optimization of the signal because was inherent to signal or because we consider will not improve the signal.

Because we want to reconstruct $B_s \to J/\psi\phi$ and $J/\psi \to \mu^+\mu^-$, $\phi \to K^+K^-$ and we have a muon detector we use the J/ψ as a pseudo-trigger. The J/ψ candidates were required to satisfy the following criteria:

- at least one reconstructed primary vertex as described in [37]. In order to be able to measure a distance since we are interested in decay lengths.

- The pair of muons making a vertex ($\chi^2 < 36$): (This give us a 1% probability therefore is a vertex)

  1. distance from primary vertex to J/ψ vertex < 10 cm. To reduce noise.
  2. no track measurements in region between primary and secondary vertex, and limited number of misses hits (<5) in the region above the secondary vertex.

- J/ψ mass > 2.9 and < 3.25 GeV; since we are only interested in the J/ψ signal.
- at least one SMT hit for each muon to warranty good vertex and save time in processing.

Once we have the J/ψ, it is combined with two tracks of opposite charge to make a vertex ($\chi^2 < 36$) of four particles. The the two tracks were required to satisfy requirements for a ϕ or K^* candidate.

- no track measurements downstream of the vertex
- at least one SMT hit for each track;
- $1.008 < \mathrm{M}(\phi) < 1.032$ GeV;
- $0.85 < \mathrm{M}(K^*) < 0.93$ GeV;
- $p_T > 0.4$ GeV for each track.

All available data up to February 27, 2004 was processed using the above criteria. We have removed all dad and special MUON, SMT and CFT runs from our analysis, using the "DZero Official Offline Run Quality Database" [38]. This was done to assure data integrity since a bad run means that data taken could have problems no detectable, for example, "fake" tracks. The procedure for evaluating MUON quality is documented in reference [39].

Luminosity was estimated scaling up the luminosity calculation made by other B-physics analysis [40]. The scale factor was 1.4, which correspond to the ratio of the amount of data we are using in comparing the data used by that analysis. The procedure was in someway rather intuitive than rigorous. A rigorous method will require a selection of an specific triggers, the problems is that if we did that we loose a few percentage of the data and since we are only doing lifetime measurements, the trigger requirement apart from that scene it is not very important. Triggers have preescale so we could not use them to calculate luminosity. One of the triggers that was fired in about 30% of our data was used in the Υ analysis, so we use it, since both analysis used the same integrated luminosity.

3.1.2 Optimization of Cuts

To clean up the B_s signal, without using direct $c\tau$ related cuts, the final cuts were optimized to yield the most significant number of B_s while trying to retain as many candidates as possible. That is, the final cuts were tuned to optimize $S/\sqrt{S+B}$ for the B_s (where S is the number of B_s signal candidates and B is the number of background events under the B_s mass peak, obtained from the sideband mass region). The optimization was done by looping over a set of parameters not related to $c\tau$, and making all possible combination of cuts at the same time. Since we already have a very significant mass peak, we do the procedure directly on data.

The final selection cuts for the B_s candidates are shown in Table 3.1.

Finally, in the cases where we had more than one candidate per event; we choose the one with the best vertex probability $P_{\chi^2}(B_s)$. For selecting the B_d candidates we used the same set of cuts as than the B_s, but apart from a few differences which arise for the different mass regions and asymmetry of the K^* final state, in comparison with the ϕ. For the mass of the K^* we are using the combination K, π which gives the closer value to the PDG.

Figure 3.1.2 shows mass distributions of the reconstructed and selected objects. For this plots an extra cut (significance of the proper decay length[1] greater than 5, e.g. $c\tau/\sigma(c\tau) > 5$) has been applied to better illustrate the objects. This cut is not applied for the rest of the analysis. Plots for ϕ and K^* mesons are shown before choosing the best vertex probability.

We also have required the proper decay length error to be less than 60 microns. The

[1] For definition of the proper decay length (PDL) see section 4.1. The uncertainty in this quantity is obtained event-by-event basis from the full covariance matrices of the tracks and the uncertainty in the position of the primary vertex.

Parameter	Cut
$p_T(B)$	> 6.5 GeV
$P_{\chi^2}(B)$	$> 1\%$
$p_T(J/\psi)$	> 4.5 GeV
$P_{\chi^2}(J/\psi)$	$> 1\%$
$p_T(\phi)$	> 2.0 GeV
$p_T(K^*)$	> 2.0 GeV
$p_T(K)$	> 0.8 GeV
$p_T(\pi)$	> 0.5 GeV

Table 3.1: Set of final cuts used to select B_s and B_d

PDL error distribution for B_s is shown in Fig 3.1.2, before this cut is applied. This cut help us eliminate some event that have very long negative lifetimes. These events made the fit very unstable not only that they are clearly non physics.

In all "B" mass computations; we use a constrained to the world average J/ψ mass [25]. The constraint is only applied to the J/ψ for computing the "B" mass. All other masses are calculated using standard invariant mass calculations without any other correction.

To get any idea of the B boost, Fig 3.1.2 shows the p_T distributions for the events in the mass signal region of B_s and B_d.

After the complete selection procedure we found 4236 B_s candidates and 30692 B_d candidates, in the mass regions defined by (5078.0-5636.0) and (4935.5-5610.5) MeV/c^2 respectively [33].

3.1.3 Monte Carlo Samples

Samples were generated using MCpythia for the production an hadronization phase, and EvtGen [34] for decaying the "b" hadrons produced. DØ release p14.05.01 was used in all cases. All B_s were forced to decay to $J/\psi+\phi$, and $J/\psi \to \mu^+\mu^-$, $\phi \to K^+K^-$, to save time. The EvtGen model to decay B_s was SVV_HELAMP with default parameter that correspond to CP even states. We also generate a sample with CP-odd parameters and other with phase space model (e.g. no polarization or CP effects) for efficiency studies. Finally, an inclusive J/ψ sample is used for resolution studies.

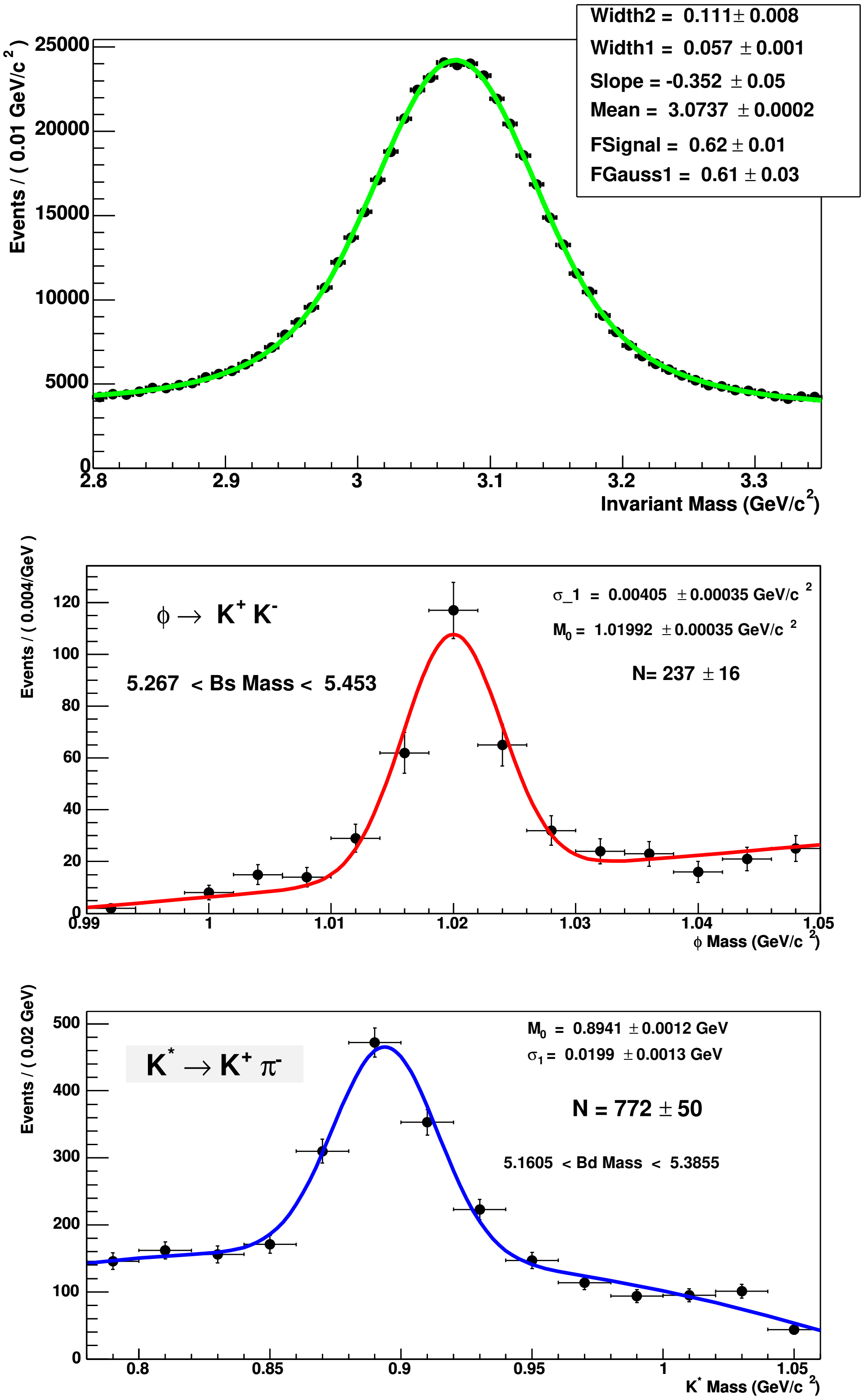

Figure 3.1: Mass distribution of reconstructed objects: J/ψ, ϕ, and K^*. A cut in the significance of the proper decay length greater than 5 has been applied. ϕ and K^* distributions before selecting the vertex with the better χ^2 are shown.

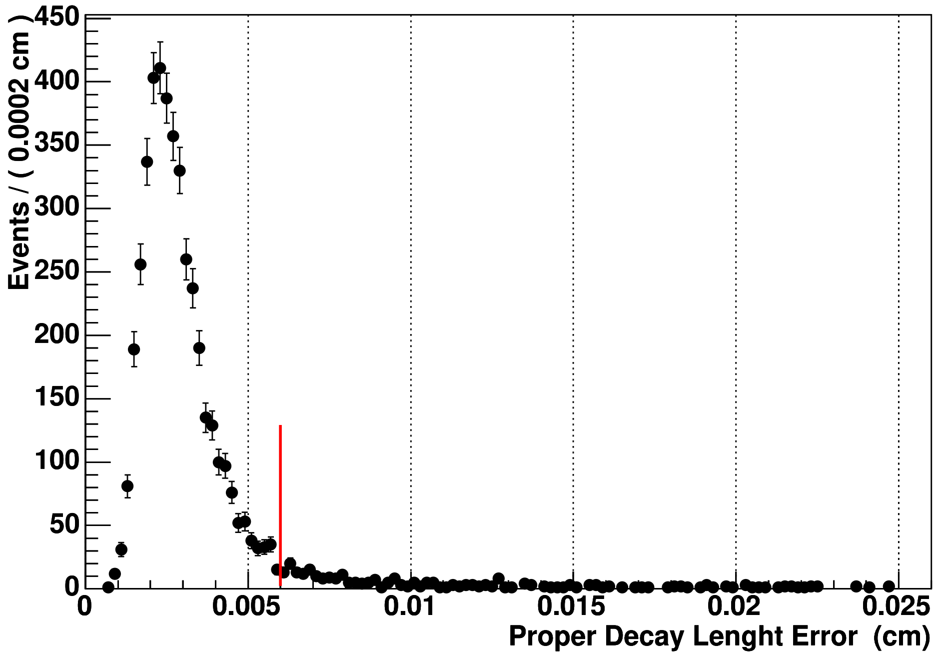

Figure 3.2: Proper Decay Length Error distribution for B_s. Red line illustrate the used cut.

The kinematic cuts applied to the samples (using DØ_mess) were: muons from J/ψ had to have $p_T > 1.5$ GeV and $|\eta| < 2.5$, and the kaons (pions) from $\phi(K^*)$ had to have $p_T > 0.3$ GeV. The sample was then processed using the standard full chain procedure DØgstar-DØsim-DØreco. The inclusive sample consist of 90,000 events.

3.1.4 Background: Cross-feed contamination

The composition of background in our final dataset, selected above, is made of a prompt components where a J/ψ from the primary vertex is randomly combined with other tracks to mimic a B decay. The second source of background comes from real heavy flavor hadrons where misreconstructed tracks and vertexes produce the same final states as in our signal. The former background component should have zero or very short lifetime, while the latter should contribute with a real long-lived component similar to our signal. Figure 3.4 shows the mass distribution for reconstructed $B \to J/\psi K^*$ from the inclusive $B \to J/\psi X$ MC sample.

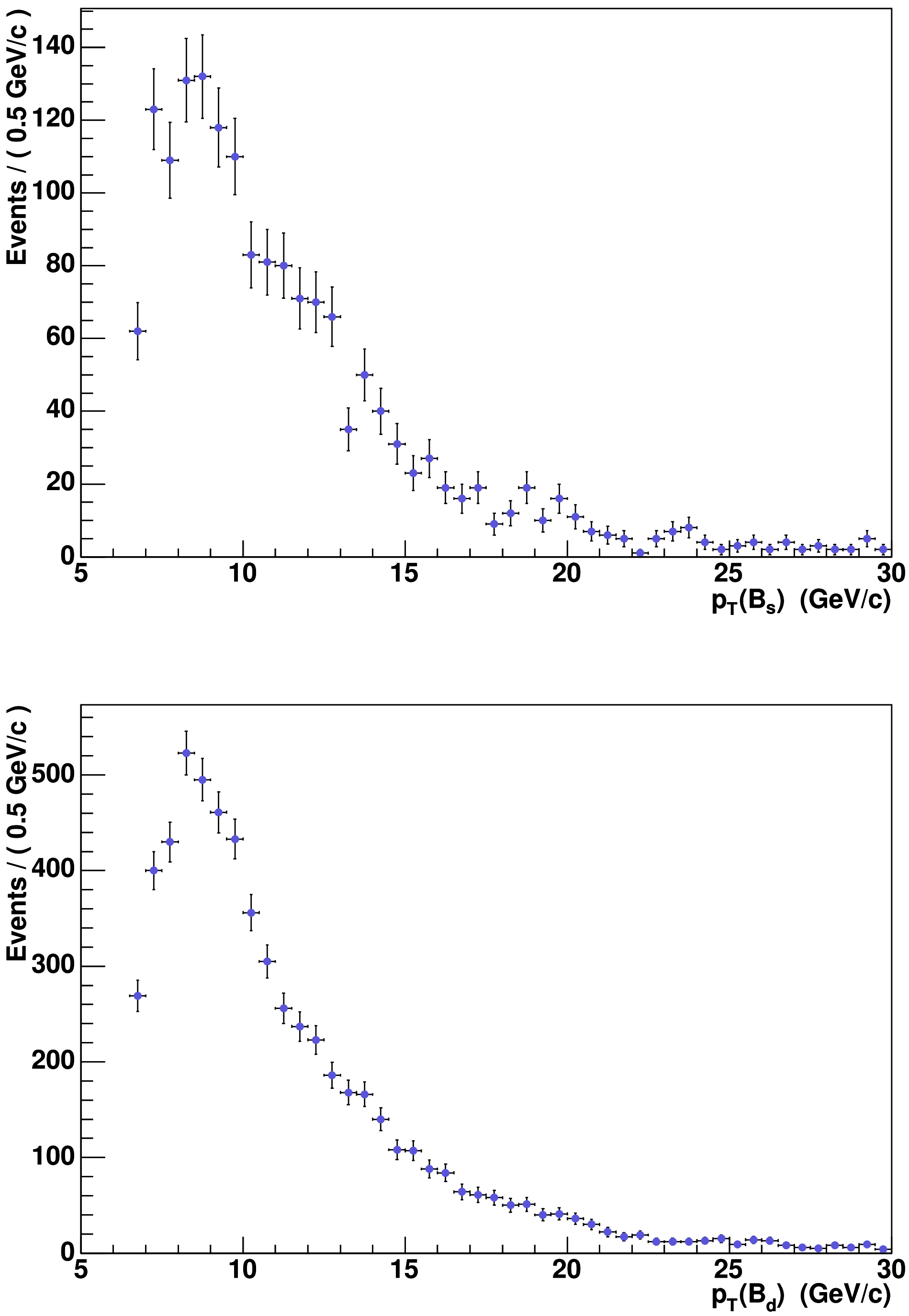

Figure 3.3: Transverse momentum distributions for events in the signal mass distribution defined as 5267.0-5453.0 MeV/c for B_s (upper) and 5160.5-5385.5 MeV/c for B_d (lower).

As can be seen, even with the limited statistics, reconstructed $J/\psi K^*$ would agreed with a Gaussian model, while the misreconstructed B are consistent with polynomial shape.

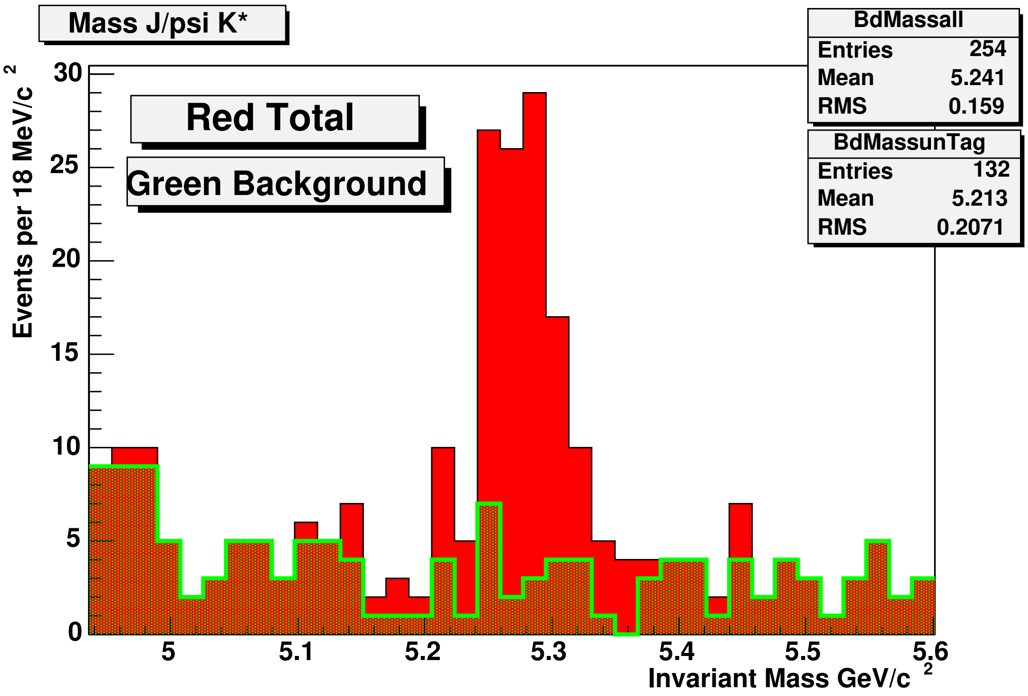

Figure 3.4: Mass distribution for reconstructed $B_d \to J/\psi(\mu^+\mu^-)K^*(K^+\pi^-)$ in an inclusive $B \to J/\psi X$ Monte Carlo sample

Part of the long-lived background component is the so called, cross-feed contamination between $B_s \to J/\psi\ (\mu^+\mu^-)\ \phi(K^+K^-)$ and $B_d \to J/\psi(\mu^+\mu^-)K^*(K^+\pi^-)$. This contamination arise from the fact that both particles have the same topology in the final state and they have similar masses. The distributions could have the same shape as our signal and then feed it, that is the reason we review them with more detail, since our background modeling could miss them. All other contributions from real heavy flavor should have distribution different to our signal and then are already taking into account in our global background modeling.

To evaluate the cross-feed contamination we generated two large MC samples, one for B_s (some 7.9M $b-\bar{b}$ events) and one for B_d (some 4.6M $b-\bar{b}$). Samples were passed to "standard" full simulation see section 2.11, Table 3.2 provide details of MC samples used. The amount of $b - \bar{b}$ generated in each case was used for normalizing the samples, then all branching ratios were adjusted to the PDG, since at generation level all them were forced to the unit. The normalization factor was (Br($B_d \to J/\psi K^*$) $\times$ Br($K^* \to K^-\pi^+$)/ (Br($B_s \to J/\psi\phi$) $\times$ Br($\phi \to K^-K^+$)) $\times$ (num. $b-\bar{b}$ for B_s / num. $b-\bar{b}$ for B_d) = 1.91 $\times$ 7.9M / 4.6M = 3.3. Figure 3.5 shows the corresponding MC mass signal plots for the reconstructed events, the contamination of the other particles is also shown. The estimated contamination was 4.40% in the B_s sample due to B_d and 1.08 % in the B_d sample due to B_s contamination. We will comeback to this evaluation when the systematic uncertainty due to the background estimation is done.

Details	B_s	B_d
Equivalent number of inclusive bb events	29.3E+10	8.9E+10
Actual number of $b\bar{b}$ events generated	7.9M	4.6M
Events filtered and full simulated	135000	253500
Br that was forced to be 1 an gen. level	0.93E−3*0.0588*0.492	1.31E−3*0.0588*0.6657
Reconstructed B_s in signal region	6677	89
Reconstructed B_d in signal region	304	8455
Normalization factor to applied	1./3.3	3.3
Number of candidates in data	337	1370

Table 3.2: Summary of MC samples used to estimate cross-feed contamination

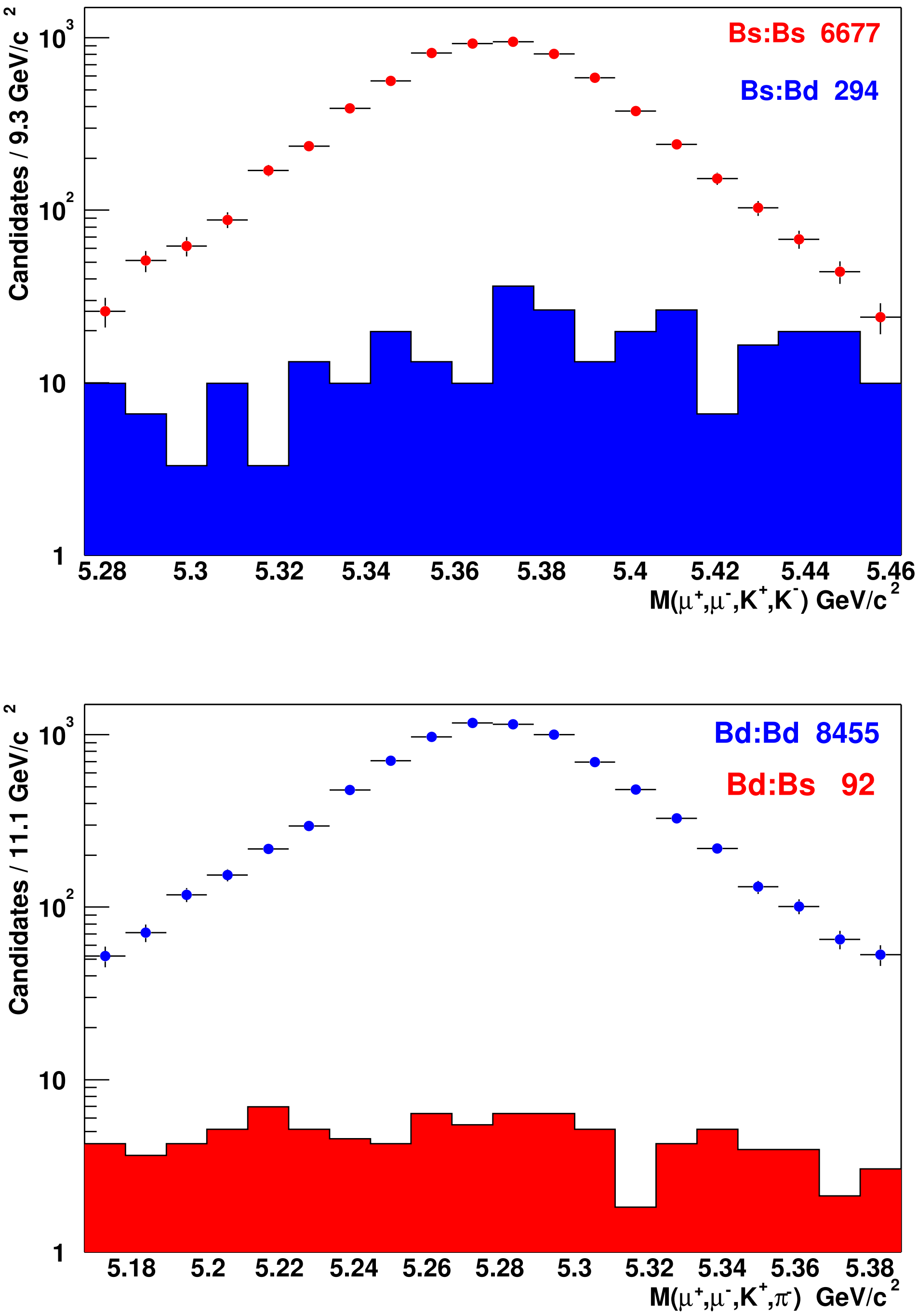

Figure 3.5: Mass distribution (histogram) for (upper): B_s when is reconstructed in a B_s and B_d sample and (lower): B_d when is reconstructed in a B_d and B_s. Numbers in the upper corners show the actual contamination.

Chapter 4

Lifetime Fit

In order to perform the lifetime fit, we have to parametrize the signal and background candidates. We parametrize both the mass and proper decay length distributions. The models used are described below.

4.1 Lifetime definition

Before explaining the models that we will use to make the measurement, it is necessary to say that what we measure the proper decay length (PDL), that is, the distance that the particle travels from the interaction point, also called primary vertex (PV) to the decay point. Known as secondary vertex (SV), in the plane (x,y) or transverse plane see figure 4.1.

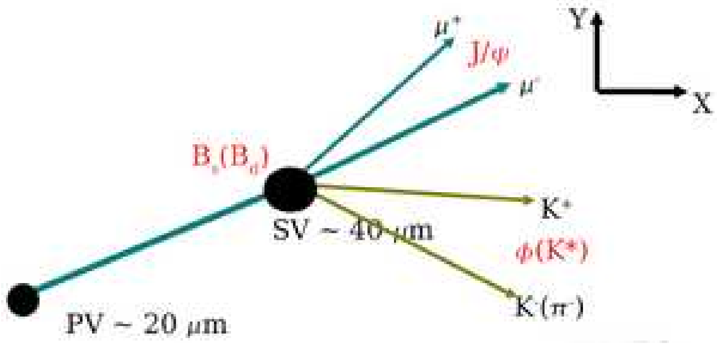

Figure 4.1: PDL Definition

4.2 Mass Model

In theory the mass signal should be a single point since the mass of the particle have a unique value. As we know, in the experiment we measure probability distributions therefore in this case the single point is a Gaussian at least for our detector resolution. The mass background is a one-degree polynomial. The reason is that we try the most simple case: if these is enough we use it, if not we go to the next more complicated.

The Probability Distribution Function (PDF) for the mass distribution was assumed to be:

$$M_{PDF}(M_j) = f_{sig} F_S^M(M_j) + (1 - f_{sig}) F_B^M(M_j) \tag{4.1}$$

where :

- f_{sig} is the fraction of signal;
- F_S^M is the PDF for the signal; and
- F_B^M is the PDF for background.

We use for the signal a normalized Gaussian distribution:

$$F_S^M(M_j) = \left(\frac{1}{\sqrt{2\pi}\sigma_M}\right) e^{\frac{-(M_j - M_0)^2}{2\sigma_M^2}}, \tag{4.2}$$

where :

- σ_M is the dispersion of the Gaussian; and
- M_0 is the mean of the Gaussian.

For the background, a first order polynomial was used as follows:

$$F_B^M(M_j) = \frac{1}{M2 - M1} - a1\left(\frac{M1 + M2}{2}\right) + a1 M_j \tag{4.3}$$

where :

- M_2 is the upper mass limit of fit range; and

- M_1 is the lower mass limit of fit range.

4.3 Proper Decay Length Model

4.3.1 Background Model

How do we know what model to use for the background?. We use what we know of the candidates that are more likely to be the background in a B meson candidate reconstruction. First we have $J\psi$ prompt. They are produced from $c\bar{c}$ interaction at the primary vertex so their lifetime should be zero, but because we have a resolution in the detector we will see it like a Gaussian centered at zero. Other component are J/ψ coming from B mesons. If the primary vertex is wrong reconstructed, we got negative or positive decay length. We use a couple of exponential decays to modelate this events. If we identified correctly the primary vertex, but the J/ψ is coming from a different B meson or decay channel. It will give us a long lifetime component. We modeled by an exponential decay about the same lifetime of the average lifetime of B candidates combined all together.

The background PDF was defined for each measured proper decay length (PDL) λ_j as

$$\begin{aligned} G_{bkg}(\lambda_j, \sigma(\lambda_j)) &= (1 - f_+ - f_{++} - f_-)R(\lambda_j, \sigma(\lambda_j)) \\ &+ f_+ \tfrac{e^{-\lambda_j/\lambda^+}}{\lambda^+} \qquad (\lambda_j \geq 0) \\ &+ f_{++} \tfrac{e^{-\lambda_j/\lambda^{++}}}{\lambda^{++}} \qquad (\lambda_j \geq 0) \\ &+ f_- \tfrac{e^{\lambda_j/\lambda^-}}{\lambda^-} \qquad (\lambda_j < 0) \end{aligned} \tag{4.4}$$

where:

λ_j	=	the PDL measurement for each data point
$\sigma(\lambda_j)$	=	the error for the PDL measurement
f_+	=	fraction of events in the positive exponential with short lifetime PDL
f_{++}	=	fraction of events in the positive exponential with long lifetime PDL
f_-	=	fraction of events in the negative exponential
λ^+	=	slope of the right exponential short lifetime PDL
λ^{++}	=	slope of the right exponential long lifetime PDL
λ^-	=	slope of the left exponential
R	=	PDF for zero lifetime,

R is also known as the resolution function. This PDF was defined as follows:

$$R(\lambda_j, \sigma(\lambda_j)) = \left(\frac{1}{\sqrt{2\pi}\sigma(\lambda_j)s}\right) e^{\frac{-(\lambda_j-\lambda_0)^2}{2(\sigma(\lambda_j)s)^2}}. \tag{4.5}$$

where:

s = correction factor to the error $\sigma(\lambda_j)$ in order to account for possible underestimate of the errors in data.

4.3.2 Signal Model

The PDF for the signal was assumed to consist of an exponential decay convoluted with a resolution function to describe the PDL of events coming from B_s or B_d. The PDF function is defined as :

$$G_{sig}(\lambda_j, \sigma(\lambda_j)) = \frac{1}{\lambda_B} e^{-\lambda_j/\lambda_B} \otimes R(\lambda_j, \sigma(\lambda_j)), \tag{4.6}$$

where:

λ_B	=	proper decay length of the B_s or B_d
R	=	is the resolution function, see equation 4.5.

4.4 Fitting Methods

The fitting method consist in defining our likelihood fit. We will describe 3 methods in the following lines. The physical results should not depend of the method.

4.4.1 Fixed Background Fit

The Fixed Background Fit (FBF) method, uses the result of the fit to the mass distribution, see equation 4.1, to define a signal region (SR), where we have signal and background events and a sideband region (SB) with background only events . Since the signal is a Gaussian, we could take the mean $\pm 2\sigma$ as the SR. For the SB, we want to be far from the Gaussian, at least 5 sigmas from the mean. While the upper and lower mass values are allowed to be as far as 9 sigmas approximately.

In the SB we will use equation (4.4). In the SR using equations (4.4) and (4.6) we have.

$$H_{FB}(\lambda_j, \sigma(\lambda_j)) = f_s G_{sig}(\lambda_j, \sigma(\lambda_j)) + (1 - f_s) G_{bkg}(\lambda_j, \sigma(\lambda_j)), \tag{4.7}$$

with:

f_s = fraction of signal events.

To get the B_s lifetime, we first fit equation (4.4) in the SB, and then fit equation in the SR.

In terms of likelihood functions, what we are using for SB is:

$$\mathcal{L}_{FB}^{SB} = \prod_j^{N_B} G_{bkg}(\lambda_j, \sigma(\lambda_j)) \quad (\forall \lambda_j \in SB), \tag{4.8}$$

and for the SR:

$$\mathcal{L}_{FB}^{SR} = \prod_j^{N_S} H_{FB}(\lambda_j, \sigma(\lambda_j)) \quad (\forall \lambda_j \in SR). \tag{4.9}$$

4.4.2 Simultaneous Fit

The second option is to perform a simultaneous fit (SF). This is similar to the fixed background fit described above, except that we fit the SB and SR at the same time, that is, we let the SR to participate in the determination of the parameters for the background. The advantage is that we take into account all correlations between parameters:

$$H_{SF}(\lambda_j, \sigma(\lambda_j)) = f_s G_{sig}(\lambda_j, \sigma(\lambda_j)) + (1 - f_s) G_{bkg}(\lambda_j, \sigma(\lambda_j)). \tag{4.10}$$

So, in these case we have only one likelihood function which is :

$$\mathcal{L}^{SF} = \begin{cases} \prod_j^{N_S} H_{SF}(\lambda_j, \sigma(\lambda_j)) \quad (\forall \lambda_j \in SR) \\ \\ \prod_j^{N_B} G_{bkg}(\lambda_j, \sigma(\lambda_j)) \quad (\forall \lambda_j \in SB). \end{cases} \tag{4.11}$$

4.4.3 Two dimensional Fit

One way to avoid the use of a-priori definition of signal and background samples is to perform a 2-dimensional fit, including an extra dimension that gives us more information to differentiate the background from the signal. In this case, the mass fit. The fit will be over a wide mass range, which we have defined as approximately ± 9 sigmas from the mean of the Gaussian, this will be defined as our fitting region (FR), and

$$\begin{aligned} H_{2D}(M_j, \lambda_j, \sigma(\lambda_j)) &= f_s F_S^M(M_j) G_{sig}(\lambda_j, \sigma(\lambda_j)) \\ &+ (1 - f_s) F_B^M(M_j) G_{bkg}(\lambda_j, \sigma(\lambda_j)). \end{aligned} \tag{4.12}$$

The likelihood function:

$$\mathcal{L}^{2D} = \prod_j^N H(M_j, \lambda_j, \sigma(\lambda_j)) \quad (\forall \lambda_j \in FR). \tag{4.13}$$

This fitting method should represent the best use of the information and will be used as main result, the other two methods described above will be used to cross-check our results.

Chapter 5

Results of the lifetime fit

5.1 B Mass Fit Results

In these section we are only interested in measuring the mass, so we apply an additional cut in the PDL significance of the B candidates. This will reduce the background and increase the significance. Note that this cut biases the PDL distribution, so, it can not be used for lifetime fit. We applied

$$c\tau/\sigma(c\tau) > 5.0, \tag{5.1}$$

where

- $c\tau$ is the PDL of the B candidate, and
- $\sigma(c\tau)$ is the error in $c\tau$.

Using the mass range 5016.0 to 5698.0 MeV/c^2 for the B_s and 4860.5 to 5685.5 MeV/c^2 for the B_d and an unbinned fit to the mass gives the result shown in Table 5.1, and 5.2. The plots of the fit are shown in Fig. 5.1.

When fitting without a significance cut the results obtained are given in Tables 5.3 and 5.4, and the plots of the fits are shown in Fig. 5.2.

Parameter	Value	Error	Units
f_{sig}	0.53	0.03	
σ_M	31.4	2.2	MeV
M_0	5360.0	2.4	MeV
$a1$	-6.95	0.65	GeV^{-3}

Table 5.1: B_s Result of the mass fit with a cut $c\tau/\sigma(c\tau) > 5.0$.

Parameter	Value	Error	Units
f_{sig}	0.35	0.01	
σ_M	37.6	1.4	MeV
M_0	5273.6	1.6	MeV
$a1$	-4.52	0.14	GeV^{-3}

Table 5.2: B_d Result of the mass fit with a cut $c\tau/\sigma(c\tau) > 5.0$.

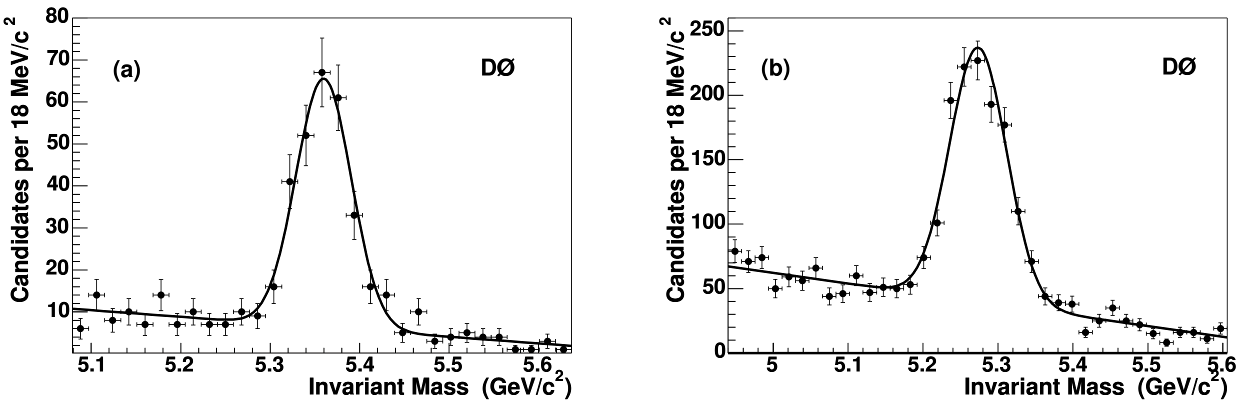

Figure 5.1: (a) B_s and (b) B_d Mass distributions with $c\tau/\sigma(c\tau) > 5.0$. N($B_s$) = 259 ± 14, N(B_d) = 1028 ± 36.

For consistency check we have fitted our mass signals in our Monte Carlo sample , using a single Gaussian and found that the widths are consistent with the ones obtained from B_s and B_d data samples. The values are 29 ± 0.3 MeV/c^2 for B_s and 36 ± 0.6 MeV/c^2 for B_d.

Parameter	Value	Error	Units
f_{sig}	0.080	0.006	
σ_M	32.9	2.4	MeV
M_0	5357.0	2.5	MeV
$a1$	-1.641	0.276	GeV^{-3}

Table 5.3: B_s Result of the mass fit with no $c\tau$ cuts.

Parameter	Value	Error	Units
f_s	0.045	0.002	
σ_M	37.9	1.4	MeV
M_0	5271.2	1.5	MeV
$a1$	-1.274	0.073	GeV^{-3}

Table 5.4: B_d Result of the mass fit with no $c\tau$ cuts.

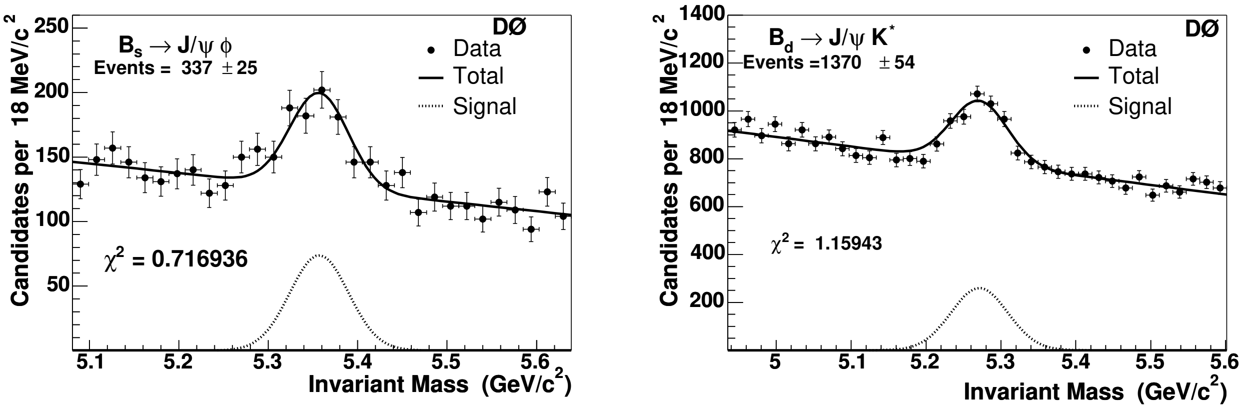

Figure 5.2: B_s and B_d Mass distributions with no $c\tau$ cuts. N(B_s) = 337 ± 25, N(B_d) = 1370 $\pm$ 54.

5.1.1 Lifetime fit results

In the next sections we will show the results obtained with the different fit methods and we will also discuss the differences between them.

5.1.2 Fixed Background Method

The results of the Fixed Background Fit Method for B_s are given in Table 5.5, using $M1 = M_0 - 2\ \sigma_M$, $M2 = M_0 + 2\ \sigma_M$ as the signal region and $[M_0 - 9\ \sigma_M, M_0 - 5\ \sigma_M]$ and $[M_0 + 5\ \sigma_M, M_0 + 9\ \sigma_M]$ as the sideband regions, where $M_0 = 5360.0$ MeV/c^2, and $\sigma_M = 31.0$ MeV/c^2 for B_s and $M_0 = 5273.6$ MeV/ c^2 , and $\sigma_M = 037.5$ MeV/c^2 for B_d. We have used MIGRAD-HESSE-MINOS to perform the fit. The $c\tau$ fit for the signal region is shown in Fig. 5.3 as well as the fit for the sideband. The likelihood scan is shown in the same figure.

The results of the the Fixed fit for B_d are given in Table 5.6. The corresponding plots are shown in Fig. 5.4. For the B_d we use the same procedure as in B_s, as well as the method to define signal and background regions.

In the rest of this thesis we will not show any other study performed using this method. We will concentrate in the 2-D Fit method. The studies made with Fixed Background Method are very similar to those shown here. At the end we will use the results in the 2-D Fit method because it gives a better statistical error (the fit has more information) and the definition of signal and background regions is not needed.

Parameter	Value	Error $-$	Error $+$	Units
f_+	0.155	-0.023	0.022	
f_{++}	0.036	-0.013	0.017	
f_-	0.074	-0.017	0.019	
λ^+	75.6	-11.5	13.6	μm
λ^{++}	324.9	-66.4	99.7	μm
λ^-	59.0	-7.6	9.8	μm
s	1.092	-0.037	0.037	
f_s	0.270	-0.017	0.018	
λ^B	432.6	-27.3	30.0	μm

Table 5.5: Result of the Fixed Background Fit to the B_s data sample.

5.1.3 Simultaneous Fit Method

The results of the the simultaneous fit for B_s are given in Table 5.7, using $M1 = M_0 - 9\sigma_M$, $M2 = M_0 + 9\sigma_M$ as the Mass window. $M1 = M_0 - 2\ \sigma_M$, $M2 = M_0 + 2\ \sigma_M$ is used as the

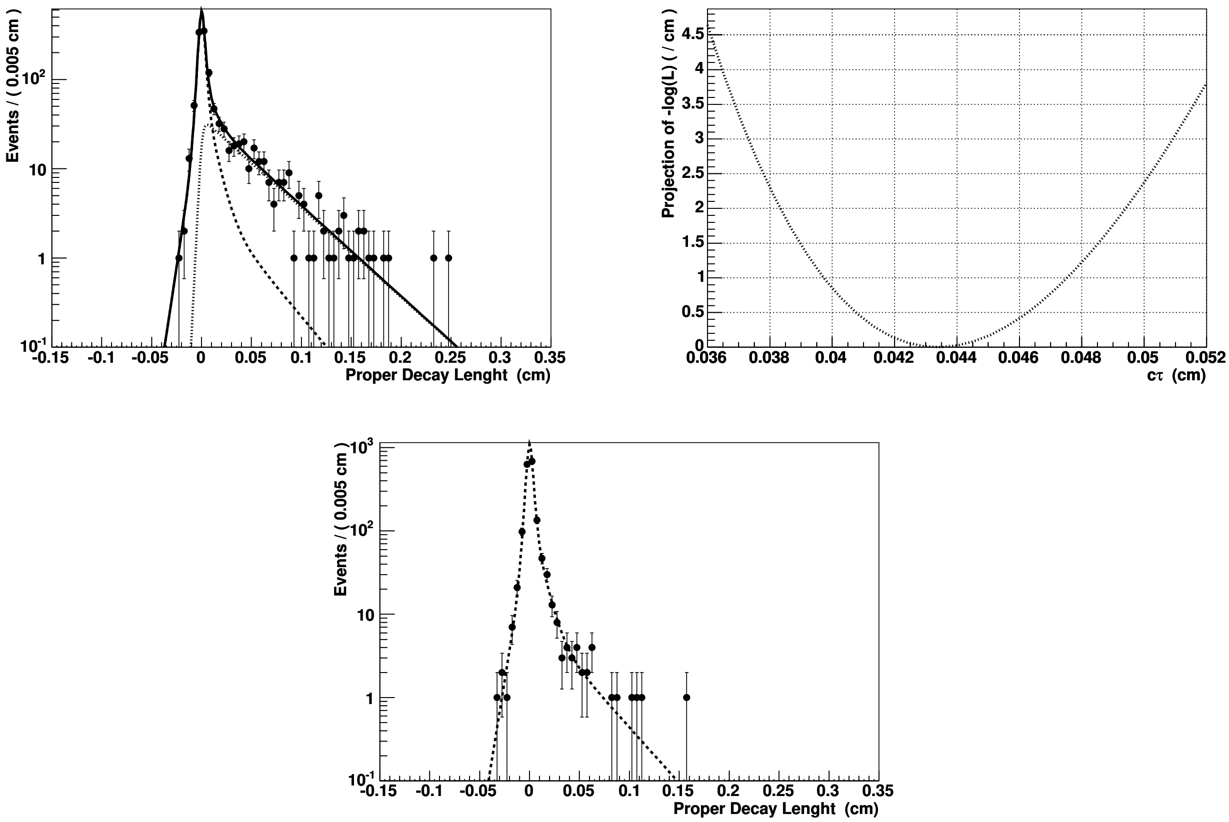

Figure 5.3: B_s Fixed Background Fit for the signal region: solid-line total, dashed-line background, dotted-line signal. Scan for the PDL parameter and Fit to the sideband region are also shown.

Parameter	Value	Error −	Error +	Units
f_+	0.147	-0.008	0.008	
f_{++}	0.039	-0.004	0.004	
f_-	0.073	-0.007	0.008	
λ^+	73.2	-4.2	4.5	μm
λ^{++}	426.9	-29.6	33.4	μm
λ^-	52.4	-2.7	3.0	μm
s	1.129	-0.015	0.015	
f_s	0.167	-0.006	0.006	
λ^B	444.5	-15.2	15.9	μm

Table 5.6: Result of the Fixed Background Fit to the B_d data sample.

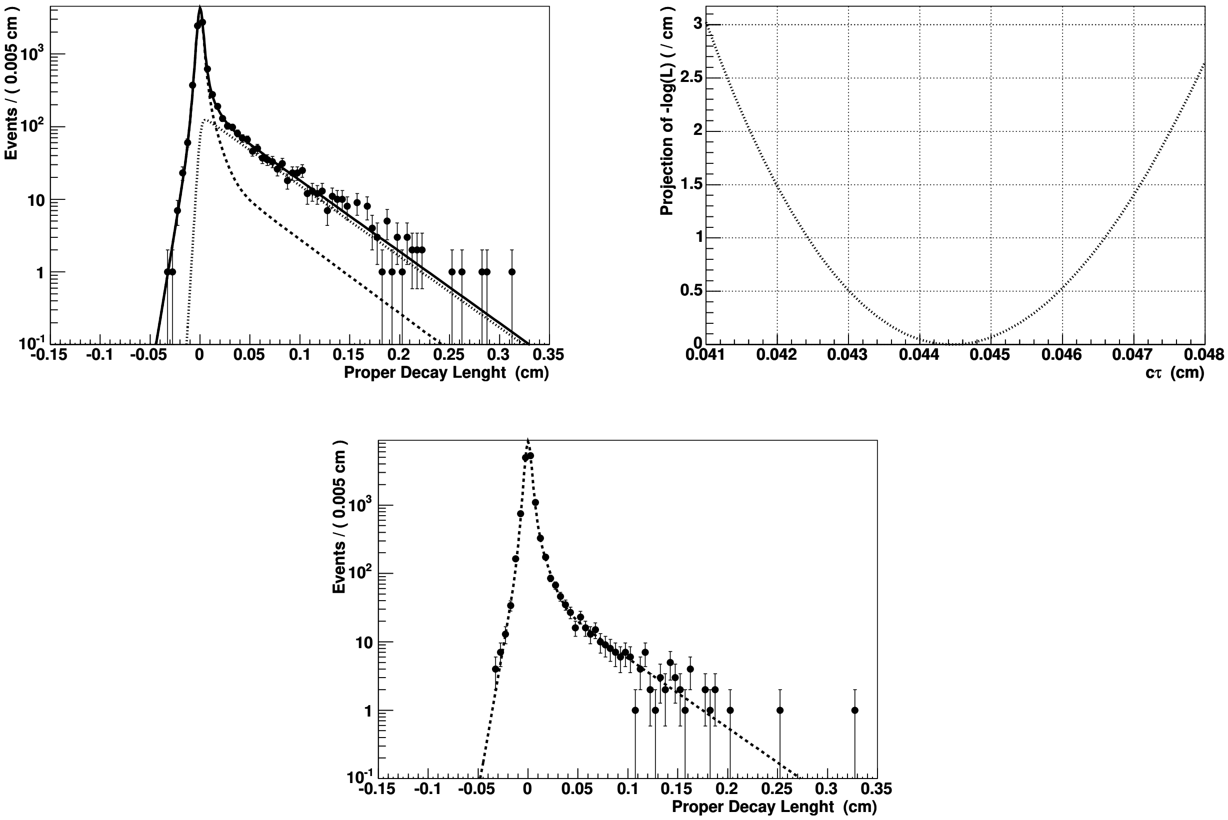

Figure 5.4: B_d Fixed Fit for the signal region: solid-line total, dashed-line background, dotted-line signal. Scan for PDL parameter as well as the Fit to the sideband region are also shown.

signal region and $[M_0 - 9\ \sigma_M, M_0 - 5\ \sigma_M]$ and $[M_0 + 5\ \sigma_M, M_0 + 9\ \sigma_M]$ as the sideband region, where $M_0 = 5360.0$ MeV/c^2 , and $\sigma_M = 31.0$ MeV/c^2 for B_s and $M_0 = 5273.6$ MeV/c^2 , and $\sigma_M = 37.5$ MeV/c^2 for B_d. We use MIGRAD-HESSE-MINOS to calculate the errors. The $c\tau$ fit for the signal region is in figure 5.5 as well as the fit for the sideband. The likelihood scan is shown in the same figure.

The results of the the simultaneous fit for B_d are shown in Table 5.8. The corresponding plots are shown in Fig. 5.6. We use the exact same procedure in fitting B_s, as well as the method to define the signal and background regions. In the rest of the text we will shown some studies performed with either this method or the fixed background method, but our main result will not be from any of these methods.

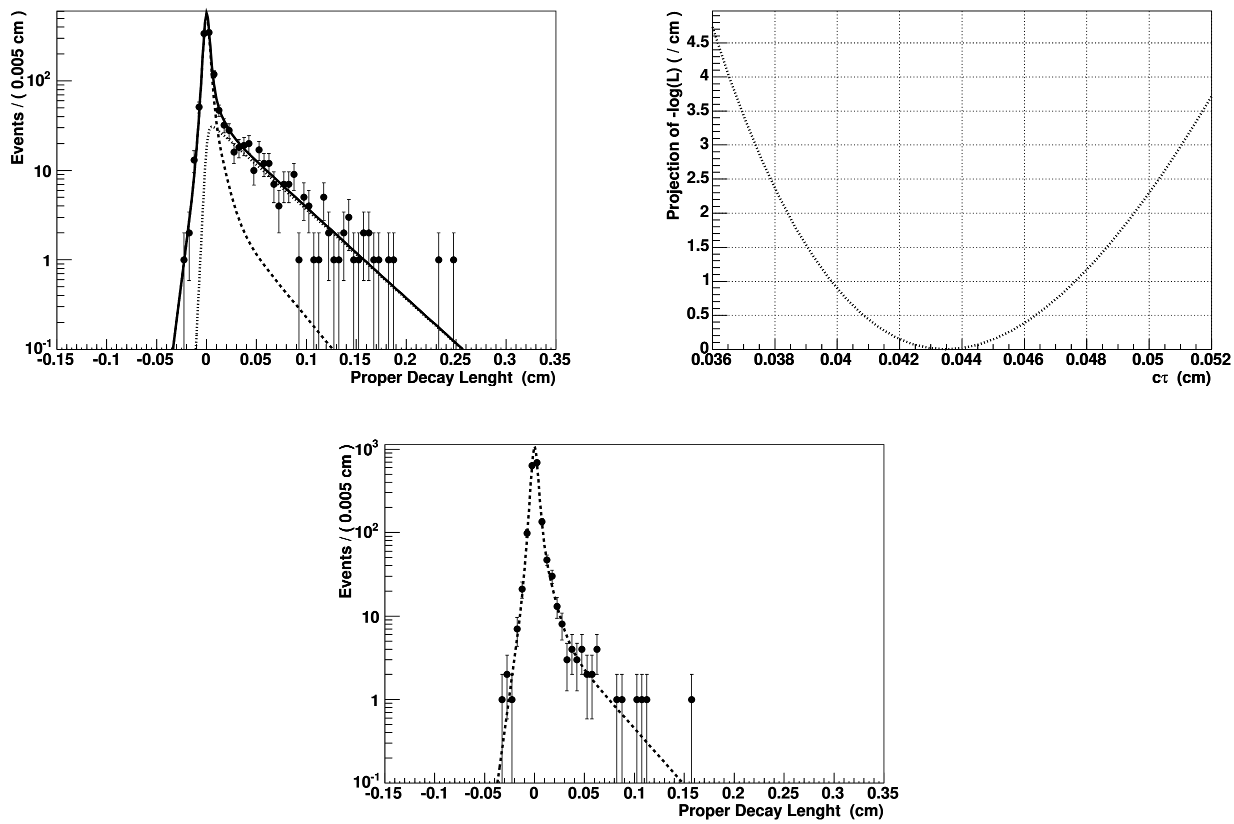

Figure 5.5: B_s Simultaneous Fit for the signal region: solid-line total, dashed-line background, dotted-line signal. Scan for the PDL parameter and Fit to the sideband region are also shown.

Parameter	Value	Error −	Error +	Units
f_+	0.164	−0.022	0.021	
f_{++}	0.038	−0.012	0.015	
f_-	0.095	−0.018	0.019	
λ^+	70.2	−9.2	10.8	μm
λ^{++}	321.7	−62.0	88.4	μm
λ^-	50.3	−4.8	6.1	μm
s	1.103	−0.033	0.034	
f_s	0.269	−0.019	0.019	
λ^B	433.6	−28.2	31.1	μm

Table 5.7: Result of the Simultaneous Fit to the B_s data sample.

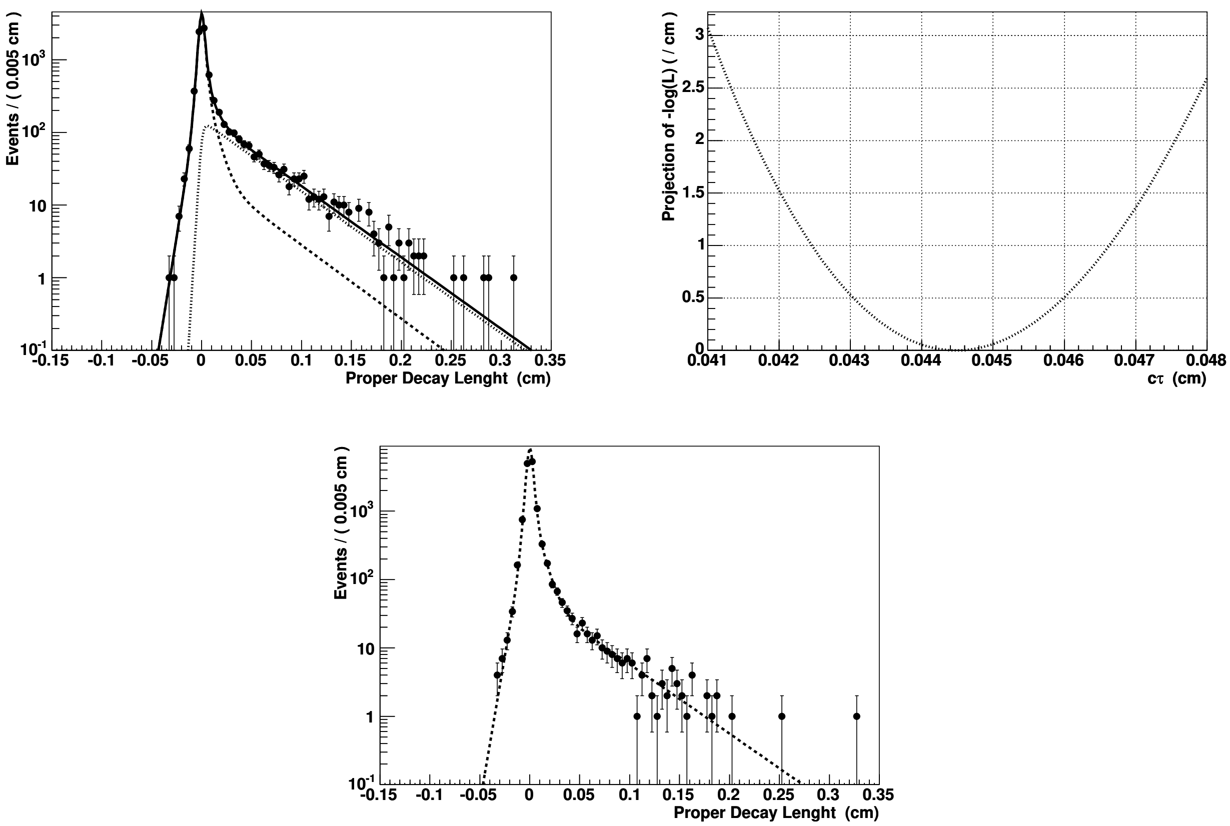

Figure 5.6: B_d Simultaneous Fit for the signal region: solid-line total, dashed-line background, dotted-line signal. Scan for PDL parameter as well as the Fit to the sideband region are also shown.

Parameter	Value	Error −	Error +	Units
f_+	0.151	−0.007	0.007	
f_{++}	0.039	−0.004	0.004	
f_-	0.076	−0.006	0.006	
λ^+	71.8	−3.6	3.8	μm
λ^{++}	427.7	−28.7	32.1	μm
λ^-	51.1	−2.2	2.4	μm
s	1.121	−0.012	0.012	
f_s	0.167	−0.007	0.007	
λ^B	444.8	−16.0	16.8	μm

Table 5.8: Result of the Simultaneous Fit to the B_d data sample.

5.1.4 2-Dimensional Fit Method

The results of the the fit for B_s are given in Table 5.9, using $M1 = M_0 - 9\ \sigma_M$, $M2 = M_0 + 9\ \sigma_M$ as the mass fitting range. We also have used MIGRAD-HESSE-MINOS to calculate the errors. The $c\tau$ fit is in Fig. 5.7 together with the fit to the mass distributions, likelihood fit scan and fit projection over the sideband mass regions.

The projection of the fit in the signal region $M1 = M_0 - 3\ \sigma_M$, $M2 = M_0 + 3\ \sigma_M$ is shown in Fig. 5.8. For the sideband regions we use $[M_0 - 9\ \sigma_M, M_0 - 3\ \sigma_M]$ and $[M_0 + 3\ \sigma_M, M_0 + 9\ \sigma_M]$. The projection over the signal region should be comparable to the fits of the signal region in the simultaneous fit method, where $M_0 = 5.3600$ MeV/c^2 , and $\sigma_M = 31.0$ MeV/c^2 for B_s and $M_0 = 5273.6$ MeV/c^2 , and $\sigma_M = 37.5$ MeV/c^2 for B_d were used.

The results of the the fit for B_d are given in Table 5.10. While the fit projections are shown in Figs. 5.9 and 5.10. We have used exactly the same method as in the B_s sample. Projections have also been defined in the same way.

5.2 Consistency checks

We performed some consistency checks, this is with the purpose to verify as best as we could possible error in our analysis. Some of them are very intuitive while other not at all. We follow the premise that if in a test we change the size of our data, for example different cuts, could not be a systematic error, since there there is also statistical fluctuation. This allows

Parameter	Value	Error −	Error +	Units
σ_M	32.9	−2.3	2.5	MeV
M_0	5357.0	−2.5	2.5	MeV
$a1$	−1.641	−0.276	0.277	GeV^{-3}
f_+	0.165	−0.016	0.016	
f_{++}	0.034	−0.009	0.011	
f_-	0.085	−0.015	0.016	
λ^+	75.0	−7.6	7.5	μm
λ^{++}	358.1	−57.0	77.7	μm
λ^-	50.6	−4.4	5.4	μm
s	1.142	−0.027	0.028	
f_s	0.080	−0.006	0.006	
λ^B	432.9	−27.0	29.5	μm

Table 5.9: Result of the 2-D fit to the B_s data sample.

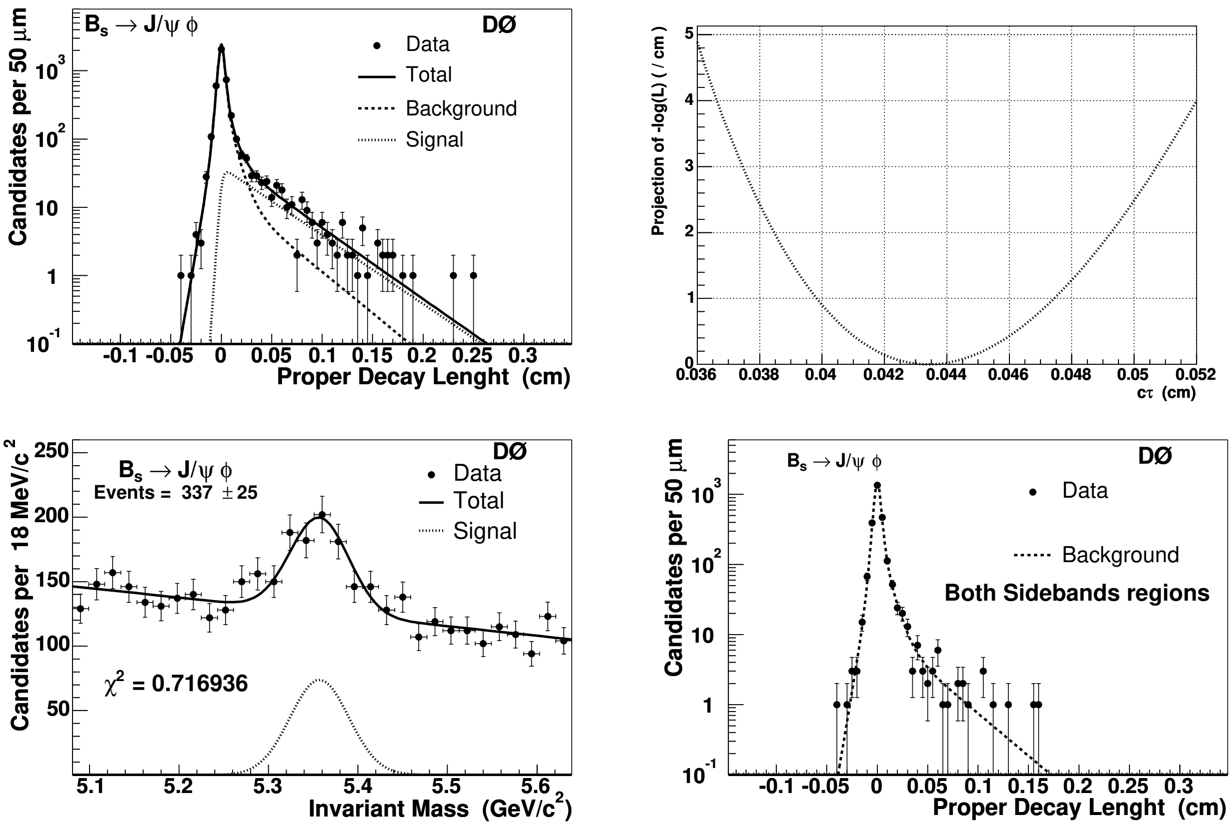

Figure 5.7: 2-D Fit projections to the B_s data: solid-line total, dashed-line background, dotted-line signal. Upper-left all mass region fit, upper-right scan for $c\tau$, lower-left mass fit, lower-right projection for the sideband region.

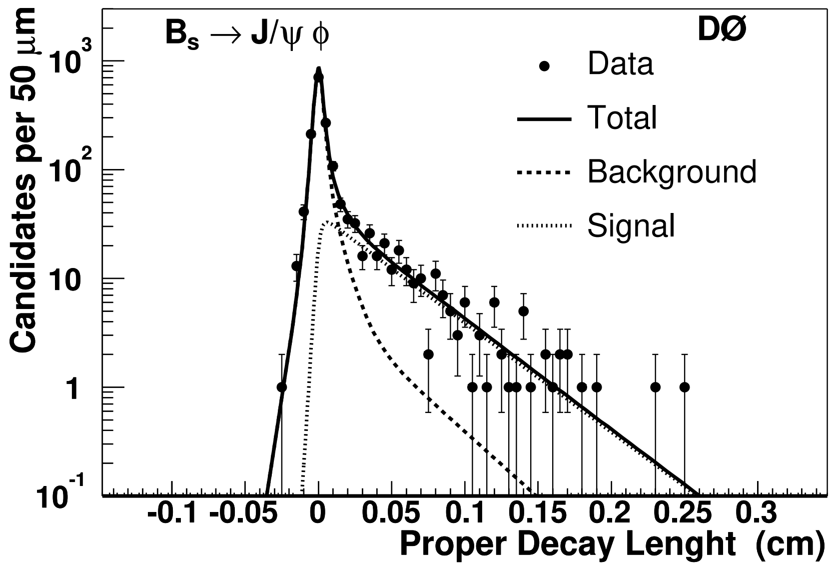

Figure 5.8: Fit projection for B_s PDL, in the signal region.

Parameter	Value	Error $-$	Error $+$	Units
σ_M	37.9	-1.3	1.4	MeV
M_0	5271.2	-1.5	1.5	MeV
$a1$	-1.274	-0.073	0.073	GeV^{-3}
f_+	0.142	-0.005	0.005	
f_{++}	0.039	-0.003	0.003	
f_-	0.067	-0.005	0.005	
λ^+	73.5	-3.1	3.3	μm
λ^{++}	426.0	-22.5	24.6	μm
λ^-	53.2	-2.0	2.1	μm
s	1.128	-0.009	0.009	
f_s	0.045	-0.002	0.002	
λ^B	441.7	-15.1	15.7	μm

Table 5.10: Result of the 2-D Fit to the B_d data sample.

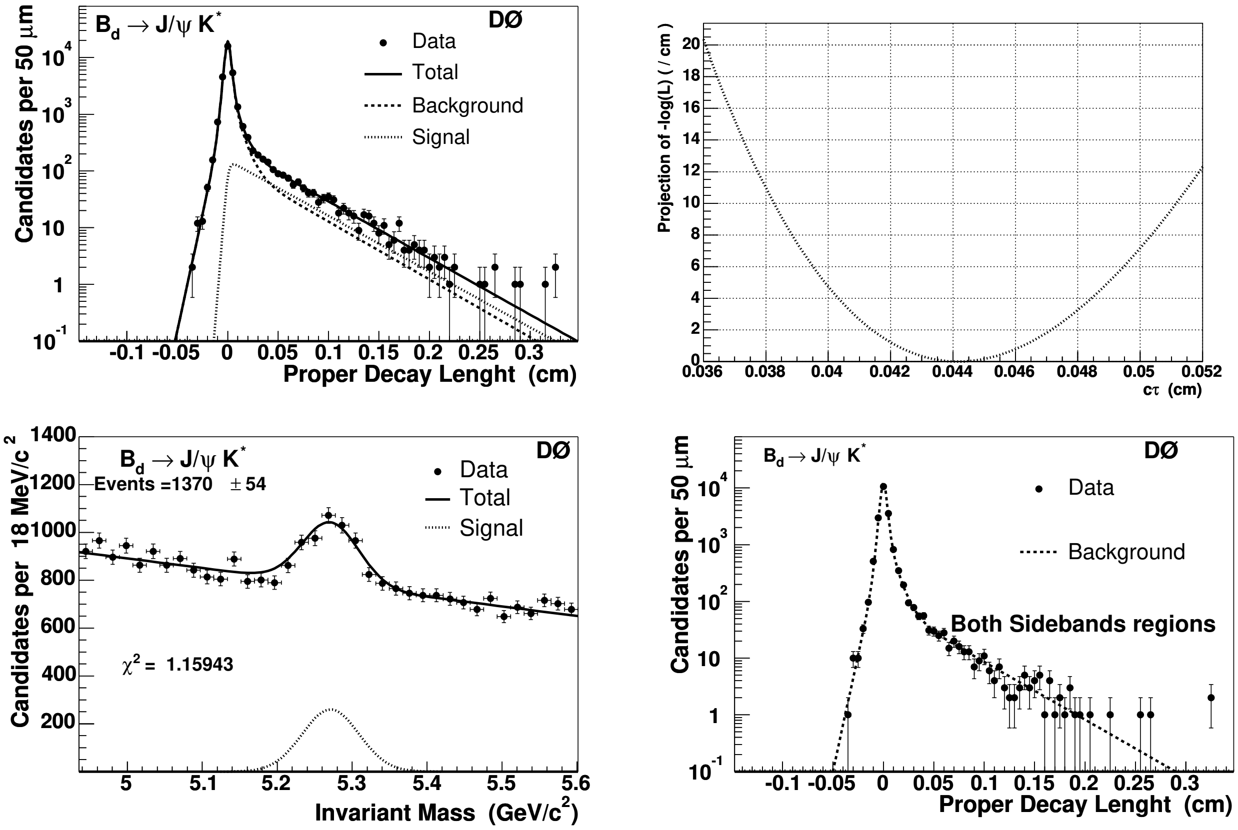

Figure 5.9: 2-D Fit projections for the B_d data. solid-line total, dashed-line background, dotted-line signal. Upper-left all mass region fit, upper-right scan for $c\tau$, lower-left mass fit, lower-right projection for the sideband region.

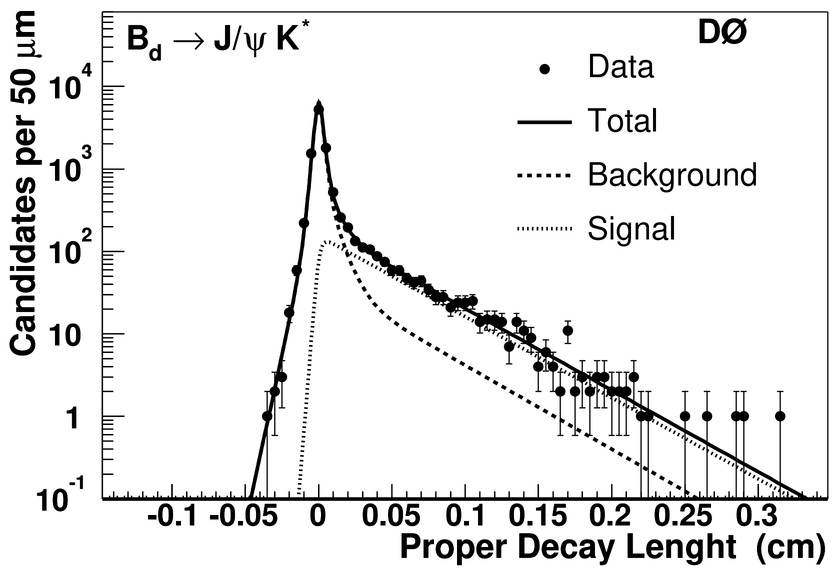

Figure 5.10: Fit projection for B_d PDL, in the signal region

us to distinguish between consistent check and systematic errors, which is difficult task. The conservation of the size of data in check is a necessary condition to be a systematic error but not sufficient.

5.2.1 Full Analysis Test

We have tested our "complete" analysis procedure, e.g., including all possible effects arising from the reconstruction program, selection procedure, performance of the vertexing package and fitting technique. We do this using a full-simulated Monte Carlo sample, where the lifetimes are known. The procedure does not provide information in the intermediate steps, (which we already have tested or done below) but about the full analysis, therefore is just a cross check. Figure 5.11 shows the likelihood fit projection PDL over the signal region when using the 2D-Fit technique, over one of our B_s MC samples. As can be seen the sample corresponds to almost signal events.

The lifetime obtained was 437.3 ± 5.4 microns (with an scale factor of 0.90 ± 0.05) when the input lifetime was 439 microns. From these numbers we do not observe any significant difference.

When the fit is forced to count only signal, i.e. just fitting a convoluted exponential decay, we observe only a negligible difference from the input value. Same behavior was observed with all other MC sample used.

5.2.2 Range of Mass selection

In the 2-Dimensional fit we use as the mass fitting region $M_0 \pm 9\sigma$, where $M_0 = 5357.0$ and $\sigma = 31.0$ MeV/c^2 for B_s and $M_0 = 5273.0$ and $\sigma = 37.5$ MeV/c^2 for B_d.

We have checked how the lifetime behaves when we change the fitting mass region. In Table 5.11 we listed the fitted $c\tau$ values for $M_0 \pm$ 6,8,9,10,11 σ. As can be seen, the maximum differences observed are within 3 (4) microns.

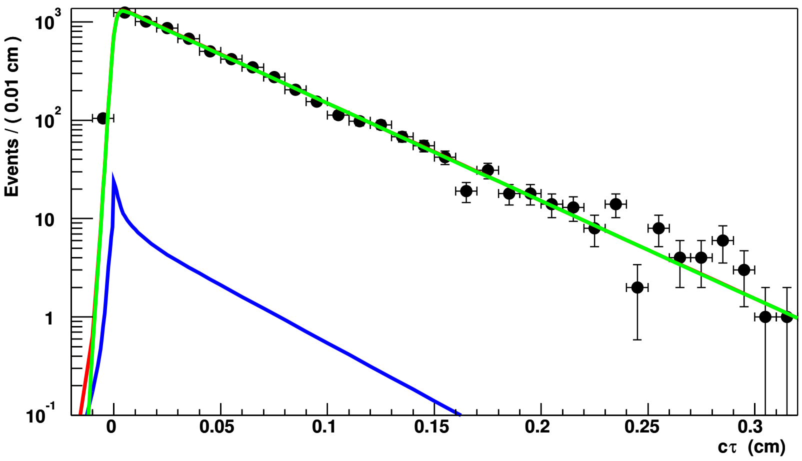

Figure 5.11: Fit projection for B_s PDL, in the signal region. Input was a fully simulated Monte Carlo Sample. Red: all contributions, green: signal, blue: combinatorial "background", mainly from miss-fitted mass distribution.

Fitting Region	$c\tau(B_s)$ (μm)	$c\tau(B_d)$ (μm)
$\pm 6\sigma$	433.2 ± 29.1	438.2 ± 15.4
$\pm 8\sigma$	432.5 ± 28.4	441.7 ± 15.2
$\pm 9\sigma$	433.9 ± 28.2	441.7 ± 15.4
$\pm 10\sigma$	432.9 ± 28.3	441.5 ± 15.4
$\pm 11\sigma$	430.4 ± 27.9	442.9 ± 15.6

Table 5.11: $c\tau$ values fitted over different mass fitting regions.

Dependence of the Mass

Given the fact that all mass peaks at DØ are slightly shifted from PDG world average values due to remaining magnetic field and material uncertainties, these could produce a small impact on our measurement (the PDL depends directly on these parameter). We have checked if this effect does not modified our measurement. For the "standard" PDL calculations we use the PDG mass value [25]. We have changed that parameter by the obtained from the fit to the mass plots, i.e., 5357.0 MeV/c^2 for B_s, and 5271.2 MeV/c^2 for B_d. We redid the fits and found differences of at up most 0.75 microns, we consider this effect negligible.

5.2.3 Different Cuts and Split Samples

We have explored two additional set of cuts: 1) The ones we obtained when we look for the maximum S/N (low statistics) and 2) the ones we obtained when looking for maximum yield (high statistics). As we mentioned before, we did not use either of these sets because one gives us a larger error, while the other has too much background which is harder to model. We decided to proceed with an intermediate option. We have also made several split sample tests which are listed on Table 5.12, and all of them look consistent.

5.2.4 Linearity of the Lifetime

We have checked if the lifetime fit is linear. To do so, we have used our MC samples and built a rejection function base of the input lifetime of the sample and a given lifetime (the desired lifetime). We have use this rejection function over the true-lifetime, if the event pass, then we build another dataset for the reconstructed lifetime of those events. The resulting dataset (which should have, at true-lifetime level, the desired lifetime) was fitted using an unbinned likelihood fit over the reconstructed lifetime. Figure 5.12 shows the result of the test. The "x" axis is the input lifetime (the desired one) and "y" is the fitting result to the reconstructed lifetime. The fit is consistent with a line of slope equal to the unity.

Particle	Check	Lifetime (μm)
B_s	cuts set1	427 ± 27
	cuts set2	435 ± 32
	run < 180956	436 ± 34
	run > 180956	428 ± 56
	$\phi(B_s) < \pi$	443 ± 38
	$\phi(B_s) > \pi$	423 ± 31
	$\eta(B_s) < 0.8$	462 ± 36
	$\eta(B_s) > 0.8$	405 ± 33
	random $< .5$	433 ± 32
	random $> .5$	432 ± 32
	sim. fit	434 ± 30
	fix sb fit	433 ± 29
B_d	cuts set 1	449 ± 15
	cuts set 2	447 ± 18
	run < 180956	442 ± 18
	run > 180956	440 ± 29
	$\phi(B_d) < \pi$	445 ± 20
	$\phi(B_d) > \pi$	436 ± 24
	$\eta(B_d) < 0.8$	427 ± 21
	$\eta(B_d) > 0.8$	453 ± 22
	random $< .5$	432 ± 22
	random $> .5$	451 ± 22
	sim. fit	445 ± 16
	fix sb fit	445 ± 16

Table 5.12: Result of the fit for different tests.

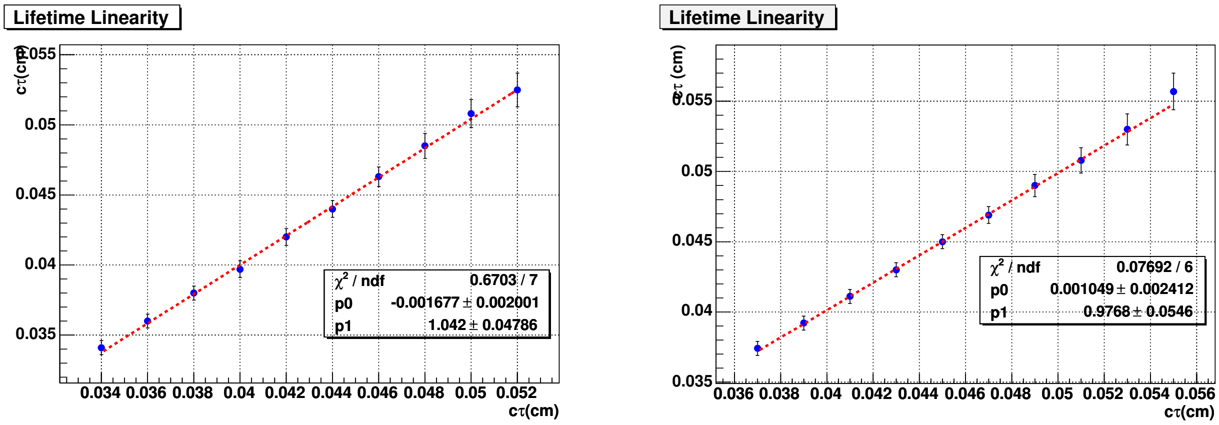

Figure 5.12: Test of the linearity of the lifetime fit. Left plot B_s MC sample was used. Right B_d MC sample was used.

5.3 Systematic Errors

In the following section we will describe what we consider the systematics errors. These are test when we do the same fit by changing some parameter in the analysis, as can be the selection of the secondary vertex, the resolution function and others detailed below. In all cases we redid the fit an compare the result with the original one.

5.3.1 J/ψ Vertex

Instead of using the B vertex, we can use the J/ψ vertex to calculate the $c\tau$. For ideal B candidates, both vertexes should be almost the same. However, since J/ψ vertex is only a two track vertex, the determination of it may be inaccurate when those two tracks are very close together (parallel). That is one of the reason we do not use that vertex for our measurement and include it as a systematic uncertainty.

In our analysis we have checked how the measurement changes when we used the J/ψ vertex. Maximum differences observed are shown in Table 5.13. Differences are not statistical significant. So far, we have chosen to use the B vertex because, this vertex should be better defined (4-track one) and has better information on the data. Figure 5.13 shows the PDL fit for B_s.

Particle	Maximum Difference (μm)
B_s	3
B_d	4

Table 5.13: Result of the fit using the J/ψ vertex.

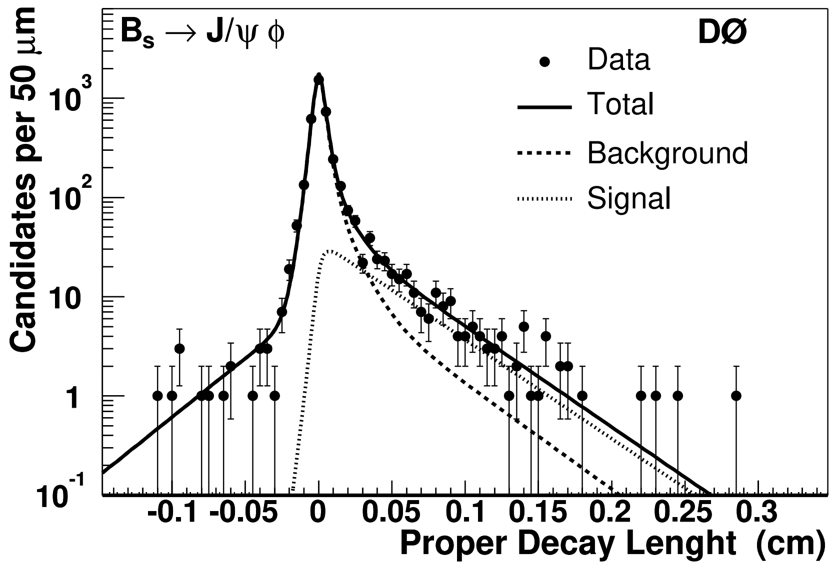

Figure 5.13: Fit to the signal candidates for B_s using the J/ψ vertex.

5.3.2 Alignment

To estimate the uncertainty due to the alignment, we use a different SMT geometry file which consists of a SMT displacement of 10 microns radially outward. The B_s candidate events were reconstructed with DØReco version p14.06.00 and the shifted geometry [43]. After that, the same selection criteria applied to the original dataset was used. The fit performed and the obtained differences are shown in Table 5.14.

Particle	Maximum Difference (μm)
B_s	2
B_d	2

Table 5.14: Systematic error from alignment. For B_d we quote the same result as for B_s.

5.3.3 Fitting

To estimate the systematic uncertainty due to the fitting procedure we generated 1000 Toy MC Samples with the same distributions used on the PDL fit and mass distributions and parameters equal to those obtained from the fits. Each sample has been generated with the same number of events as in each data sample. If we are not introducing any bias to the measurement we should see the average fitted $c\tau$ to those Toy MC samples equal to the input $c\tau$ value.

After performing the test we found that the average fitted $c\tau$ distributions were shifted by 0.3 ± 0.9 μm for B_s and 0.2 ± 0.5 μm for B_d when compared to the input $c\tau$ value. The width of the fitted $c\tau$ distribution was found to be 28.3 ± 0.6 μm and 15.3 ± 0.3 μm respectively, consistent with the statistical error of the measurement. Figure 5.14 shows the distribution of fitted $c\tau$ of the toy MC samples.

We neglect any systematic uncertainty due to our fitting technique.

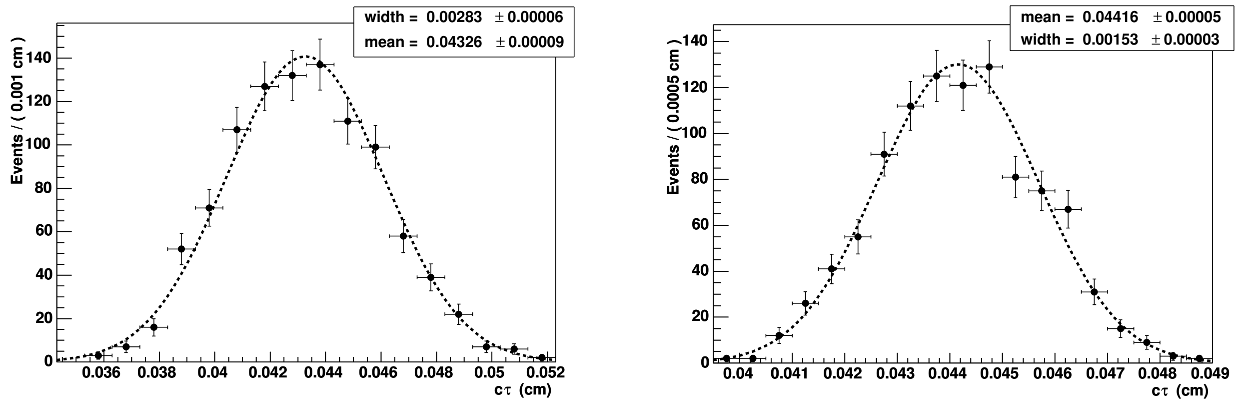

Figure 5.14: Distributions of the fitted $c\tau$ for toy MC samples: left B_s, right B_d.

5.3.4 Background

To study the effect of the background modeling on our measurement we considered the following criteria:

A- Convoluted the exponential decays in the background with the same resolution function used in the signal decay. In other words we assumed "the decays in the background also have resolution".

B- Use a second order polynomial for the background shape of the mass distribution.

C- Modified the functional form of the Lifetime Model. To account for discrepancies on the estimation of the background we have fitted separately the PDL distributions of the lower and high mass region. Prompt and short lifetime components have been fixed to the values obtained in the fit to the complete fitting range mass. Fit values obtained are shown in Table 5.15. Using the lifetime values obtained we modified the Model of background to included two long-lived components, with a relative fraction between them

$$f_{++}\left(\frac{f_{LL}}{\lambda^{lo}}e^{-\lambda_j/\lambda^{lo}} + \frac{(1-f_{LL})}{\lambda^{hi}}e^{-\lambda_j/\lambda^{hi}}\right).$$

This ratio (f_{LL}) can be either a floating parameter or a fixed value. As floating parameter we found to be $0.98^{+0.02}_{-0.36}$ for B_s and $0.78^{+0.20}_{-0.16}$ for B_d, which are very well consistent to the ones obtained when performing simple weighting average of values obtained from the two mass regions shown in Table 5.15: $0.062 * 1417/(0.062 * 1417 + 0.006 * 1147) = 0.93$ for B_s and $0.057 * 11024/(0.057 * 11024 + 0.019 * 8704) = 0.79$ for B_d. To evaluate the associated systematic uncertainty we have fixed f_{LL} to the fitted values $\pm 1\sigma$. The obtained values are listed in Table 5.16. We took the maximum deviation as the systematic uncertainty.

D- In the study shown in section 3.3 we did not observe any structure in the mass distribution due to the cross-feed contamination. This background should have the bigger contribution among all backgrounds from misreconstructed heavy hadrons, then we can safely assume they are already taken into account in our background modeling, thus neglect any effect from this source.

Results of all background estimates are given in Table 5.17.

	Lower mass region			High mass region		
	Lifetime (μm)	Fraction (%)	Entries in Region	Lifetime (μm)	Fraction (%)	Entries in Region
B_s	335 ± 57	6.2 ± 1.4	1417	540 ± 336	0.6 ± 0.4	1147
B_d	452 ± 25	5.7 ± 0.4	11024	263 ± 36	1.9 ± 0.4	8704

Table 5.15: Lifetime and fraction of the Long-lived component, as obtained from individual lifetime fits, in each mass region.

	fraction f_{LL} (B_s)	$\Delta c\tau$ (μm) (B_s)	fraction f_{LL} (B_d)	$\Delta c\tau$ (μm) (B_d)
Fixed (w.ave.)	0.93	0.0	0.79	-0.2
Float	$0.98^{+0.02}_{-0.36}$	$+0.8$	$0.78^{+0.20}_{-0.16}$	0.0
Fixed ($+\sigma$)	1.00	$+1.0$	0.98	-2.2
Fixed ($-\sigma$)	0.62	-2.5	0.62	$+2.6$

Table 5.16: Deviations observed as the fraction of the Long-lived component is modified.

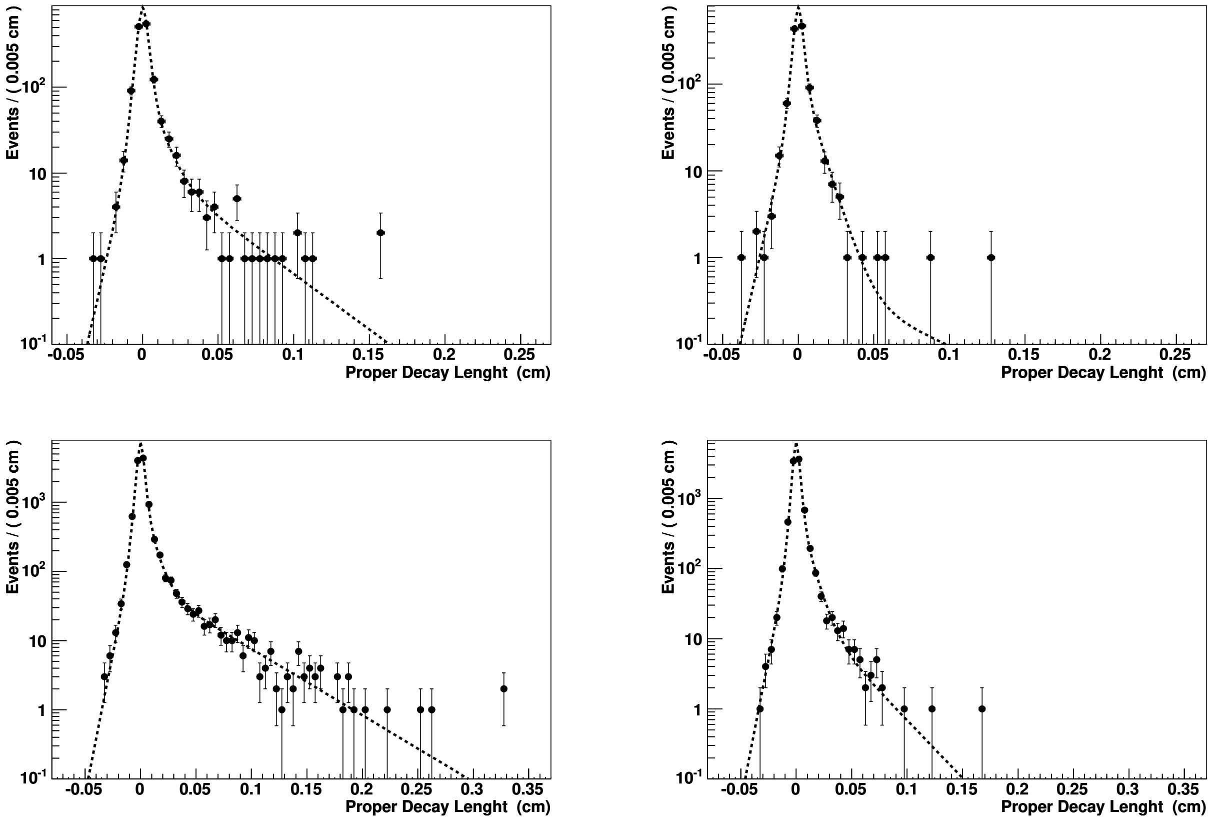

Figure 5.15: Fitted PDL distributions for low (left) and high (right) mass regions for B_s (upper) and B_d (lower).

Particle	Differences (μm)
B_s	$1 \oplus 2 \oplus 3 = 4$
B_d	$1 \oplus 4 \oplus 3 = 5$

Table 5.17: Summary of the background contributions. Contributions were added in quadrature and rounded.

5.3.5 Resolution Model

To study the effect of uncertainties in our resolution model, we modified the functional form of a Gaussian weighted by the event-by-event PDL errors to a 2 Gaussian weighted by the event-by-event errors with two different "s" scale factors and a relative ratio between them, which is a floating parameter in the fit. The fitted values for those parameters are $s_1 = 0.94 \pm 0.08$, $s_2 = 1.82 \pm 0.18$ and $f = 0.63 \pm 0.12$ for B_s, and $s_1 = 0.99 \pm 0.02$, $s_2 = 2.17 \pm 0.08$ and $f = 0.76 \pm 0.02$ for B_d. The maximum differences observed in the lifetime fit are listed in Table 5.18.

Particle	Maximum Difference (μm)
B_s	3
B_d	3

Table 5.18: Lifetime differences when different resolution function parameterizations are used. Values correspond to maximal absolute differences.

5.3.6 Systematics uncertainties Summary

In Table 5.19, we have summarize all systematics uncertainties mentioned above and the added them in quadrature.

Source	$B_s \to J/\psi\phi$	$B_d \to J/\psi K^*$	τ_s/τ_d
Alignment	2	2	0.000
J/ψ vertex	3	4	0.002
Resolution model	3	3	0.000
Background model	4	5	0.002
Total	**6**	**7**	**0.003**

Table 5.19: Summary of systematic uncertainties

5.4 Lifetime Ratio

Using the measured numbers for $c\tau(B_s)$ and $c\tau(B_d)$, we determined the lifetime ratio:

$$\frac{\tau_{B_s}}{\tau_{B_d}} = 0.980\ ^{+0.075}_{-0.070}\ (\text{stat.})\ \pm 0.003\ (\text{syst}), \tag{5.2}$$

The statistical uncertainties were propagated in quadratures, and the systematic uncertainty was evaluated by adding each contribution to the corresponding central one, and evaluating a new ratio, with the difference from the nominal value taken as the systematic uncertainty of that source as shown in Table 5.19. The sum in quadrature of all contributions is reported as the overall systematic uncertainty on the ratio of lifetimes.

Chapter 6

Results and Conclusions

Using an integrated luminosity of approximately 220 pb^{-1}, we have measured the B_s lifetime in the decay channel $J/\psi\phi$ and the B_d lifetime in the decay channel $J/\psi\ K^*$:

$$c\tau(B_s) = 432.9^{+29.5}_{-27.0}\ \text{(stat)} \pm 6.0\ \text{(syst)}\ \mu\text{m}, \tag{6.1}$$

$$\tau(B_s) = 1.444^{+0.098}_{-0.090}\ \text{(stat)} \pm 0.020\ \text{(syst)}\ \text{ps}. \tag{6.2}$$

$$c\tau(B_d) = 441.7^{+15.7}_{-15.1}\ \text{(stat)} \pm 7.0\ \text{(syst)}\ \mu\text{m}, \tag{6.3}$$

$$\tau(B_d) = 1.473^{+0.052}_{-0.050}\ \text{(stat)} \pm 0.023\ \text{(syst)}\ \text{ps}. \tag{6.4}$$

Both numbers are in good agreement with the current world average (PDG) values: $\tau(B_s) = 1.461 \pm 0.057$ and $\tau(B_d) = 1.536 \pm 0.014$. Table 6.1 shows most recent measurements made by several experiments. The B_s lifetime measurement is the world's current best measurement from a single experiment with fully reconstructed B mesons. The ratio is also in very good agreement with the QCD models based on heavy quark expansion, which predicts a difference between B_s and B_d lifetimes of the order of 1% [26]. The lifetime ratio measured was:

$$\frac{\tau_{B_s}}{\tau_{B_d}} = 0.980 \ ^{+0.075}_{-0.070} \text{ (stat) } \pm 0.003 \text{ (syst).} \tag{6.5}$$

Experiment	B_s	B_d
World Average(PDG)	1.461 ± 0.057	1.536 ± 0.014
This Measurement	$1.444^{+0.098}_{-0.090} \pm 0.020$	$1.473^{+0.052}_{-0.050} \pm 0.023$
CDF (Run II) prelim.	$1.369 \pm 0.100^{+0.008}_{-0.010}$	$1.539 \pm 0.051 \pm 0.008$
BaBar	–	$1.523^{+0.024}_{-0.023} \pm 0.022$
BELLE	–	$1.554 \pm 0.030 \pm 0.019$
CDF (Run I)	$1.36 \pm 0.09^{+0.06}_{-0.05}$	$1.497 \pm 0.073 \pm 0.032$
DELPHI	$1.42^{+0.14}_{-0.13} \pm 0.03$	$1.532 \pm 0.041 \pm 0.040$
OPAL	$1.50^{+0.16}_{-0.15} \pm 0.04$	$1.541 \pm 0.028 \pm 0.023$
ALEPH	$1.47 \pm 0.14 \pm 0.08$	$1.518 \pm 0.053 \pm 0.034$

Table 6.1: Previous lifetime measurements. (Numbers were taken from ref. [1], except CDF Run II result)

The study performed here shown that the DØ collaboration is ready to make significant contribution to the understanding of the Standard Model. Soon more exciting results are to come.

Appendix A

Resolution Studies

To make sure that our vertexing implementation does not produce a significant bias in the lifetime measurement we have performed a resolution study, which is shown below.

A.1 Primary vertex reconstruction

Once we have a J/ψ in the sample the next step is to find a primary vertex. Primary vertex is reconstructed event-by-event basis using selected tracks and the beam spot position as a constraint. The beam spot is calculated as the run-by-run beam average position, where a typical run last several hours. The tracks used in the primary vertex are those well measured tracks that does not come from any long lived decays or have interact with the material of the detector to avoid any possible bias. A more detailed description of the vertexing algorithm can be found in Ref. [37].

To validate the vertexing implementation, we have used an inclusive J/ψ Monte Carlo sample, because it is the one matching our data best at this stage (a reconstructed J/ψ in the event).

Figure A.1 shows resolution distributions for the found primary vertex along the x, y and z axes. Numbers are consistent with expectations. We do not observe a bias. Pull distributions in Fig. A.2 are very close to the unity. Pull distributions are defined as (Reco-Generated)/Error(Reco) for each variable.

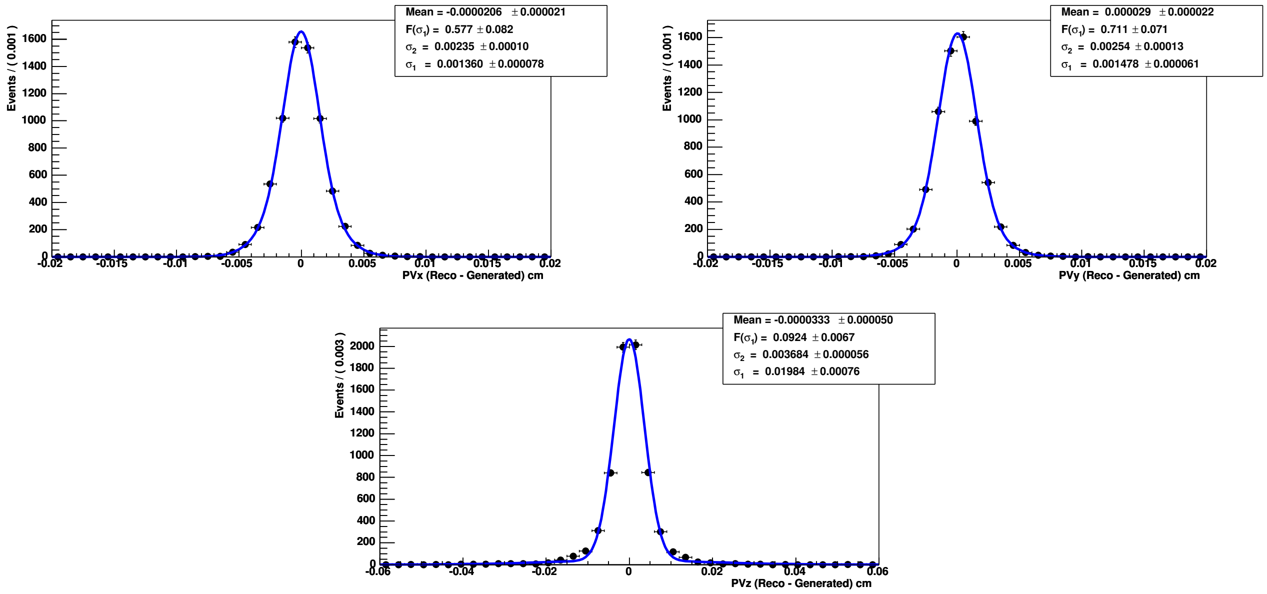

Figure A.1: Primary Vertex Resolution: (top left) x coordinate, (top right) y coordinate and (bottom) z coordinate.

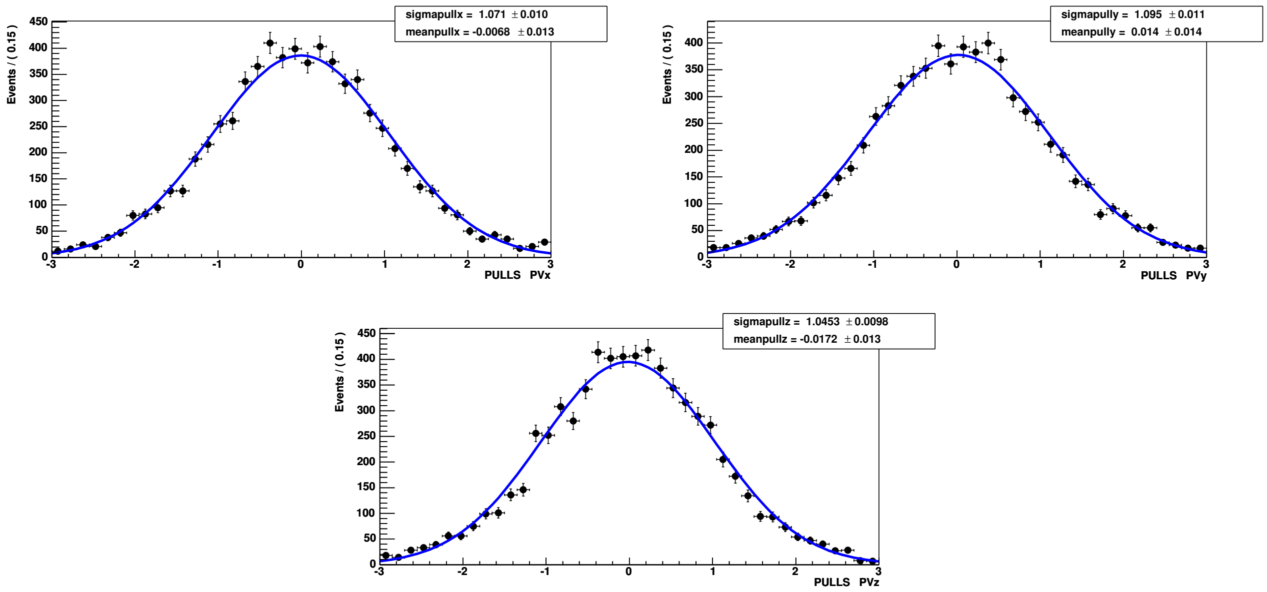

Figure A.2: Primary Vertex pulls: (top left) x coordinate, (top right) y coordinate and (bottom) z coordinate.

A.2 J/ψ Vertex

Using the same Monte Carlo sample; we produced the J/ψ vertex resolution distributions shown in Fig. A.3, again we do not observe a bias. Pulls distributions are in Fig. A.4.

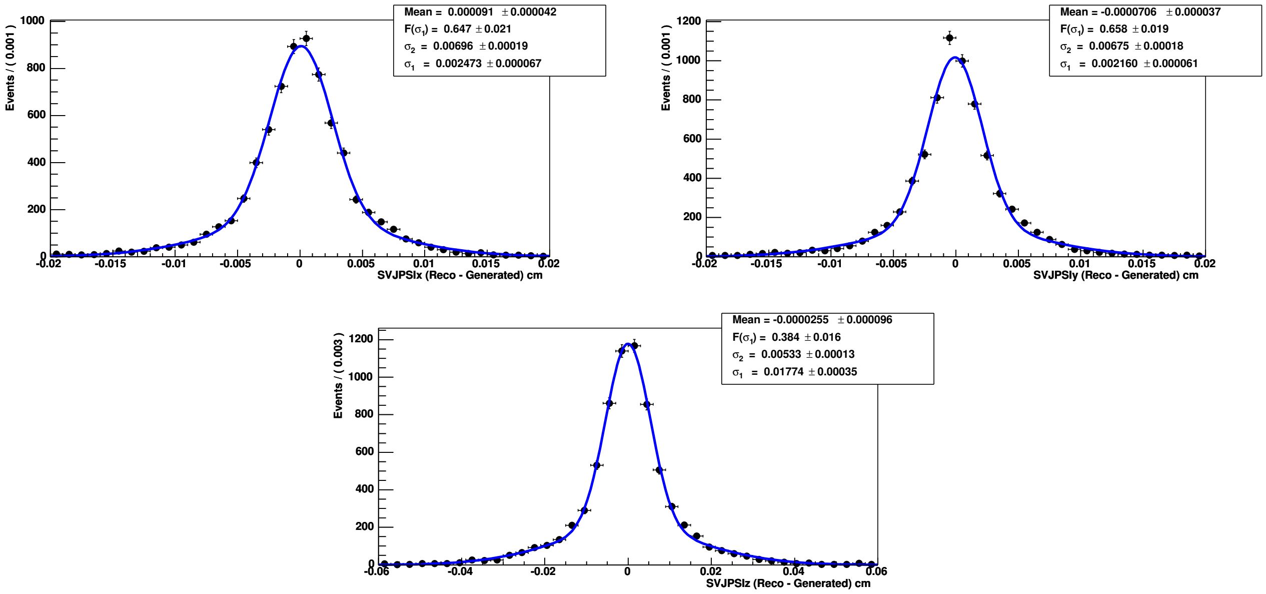

Figure A.3: J/ψ Vertex Resolution: (top left) x coordinate, (top right) y coordinate and (bottom) z coordinate.

A.3 B_s and B_d Vertex

To test the B vertex,that is the one we will be using, we have used the $B_s \to J/\psi\phi$ ($B_d \to J/\psi K^*$) Monte Carlo samples. From them we obtained the resolution distributions shown in Fig. A.5. Pulls distributions are shown in Fig. A.6.

A.4 Proper decay length

We performed the same study for proper decay length (PDL) distributions of B_s and B_d particles. The PDL is defined as the ratio of the mass of the B to the reconstructed transverse momentum times the "signed" transverse length i.e., $\lambda_B = L_{xy}(M_B/p_T)$, where

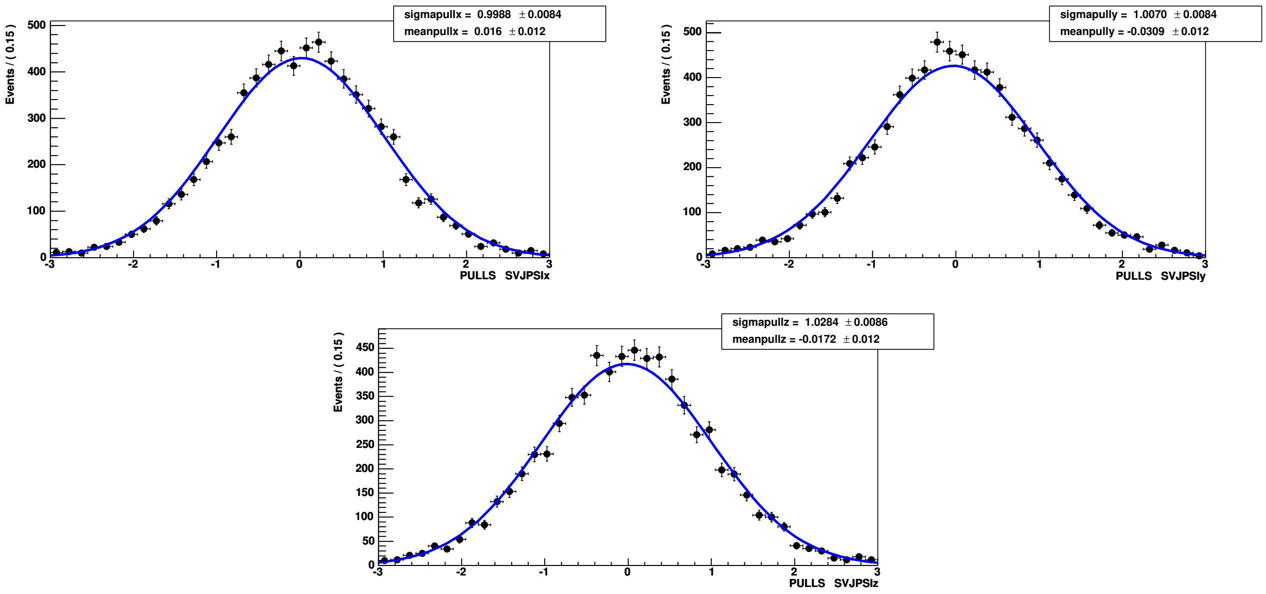

Figure A.4: J/ψ Vertex pulls: (left) x coordinate, (center) y coordinate and (right) z coordinate.

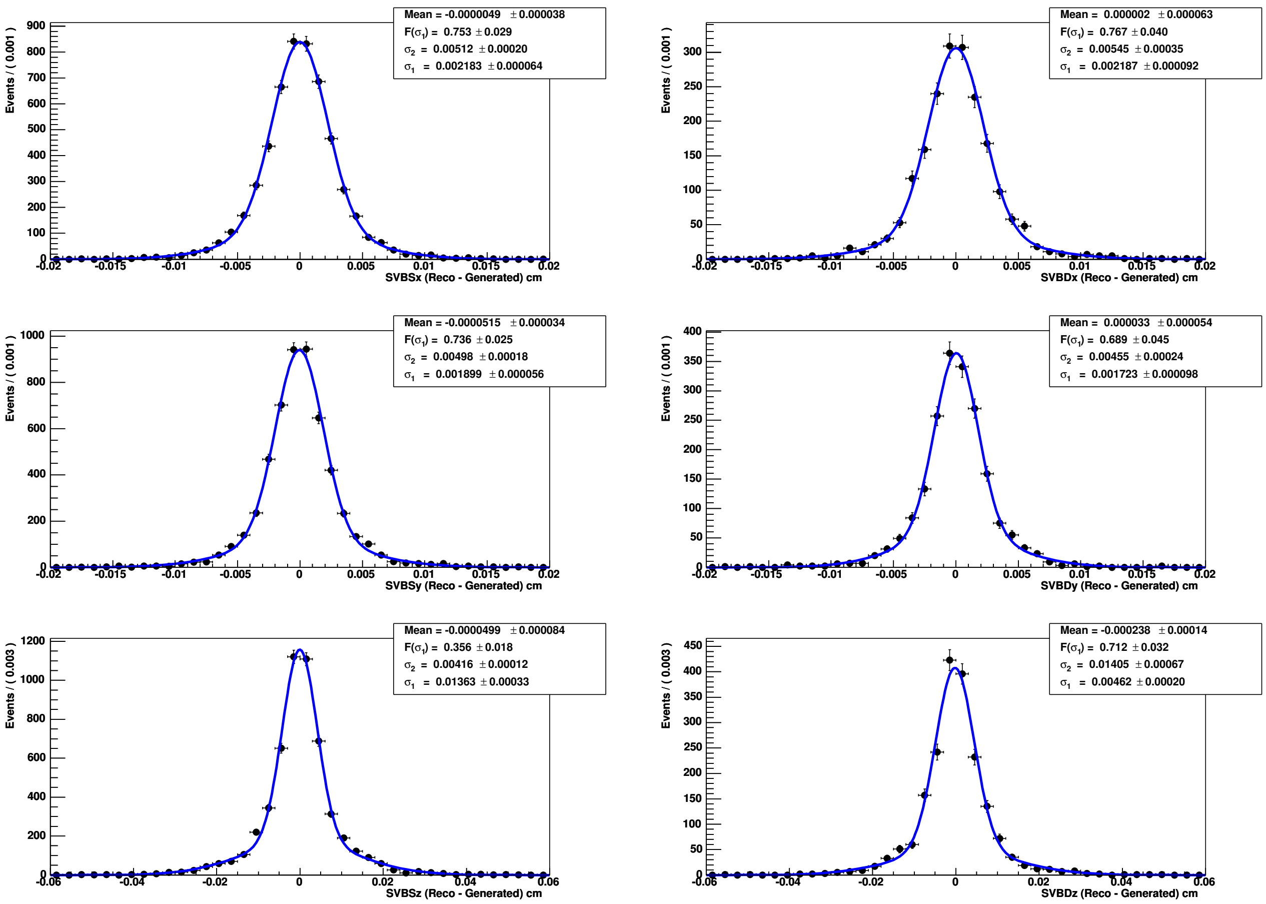

Figure A.5: Secondary Vertex Resolution: (top row) x coordinate, (medium row) y coordinate and (bottom row) z coordinate. left column B_s, right column B_d.

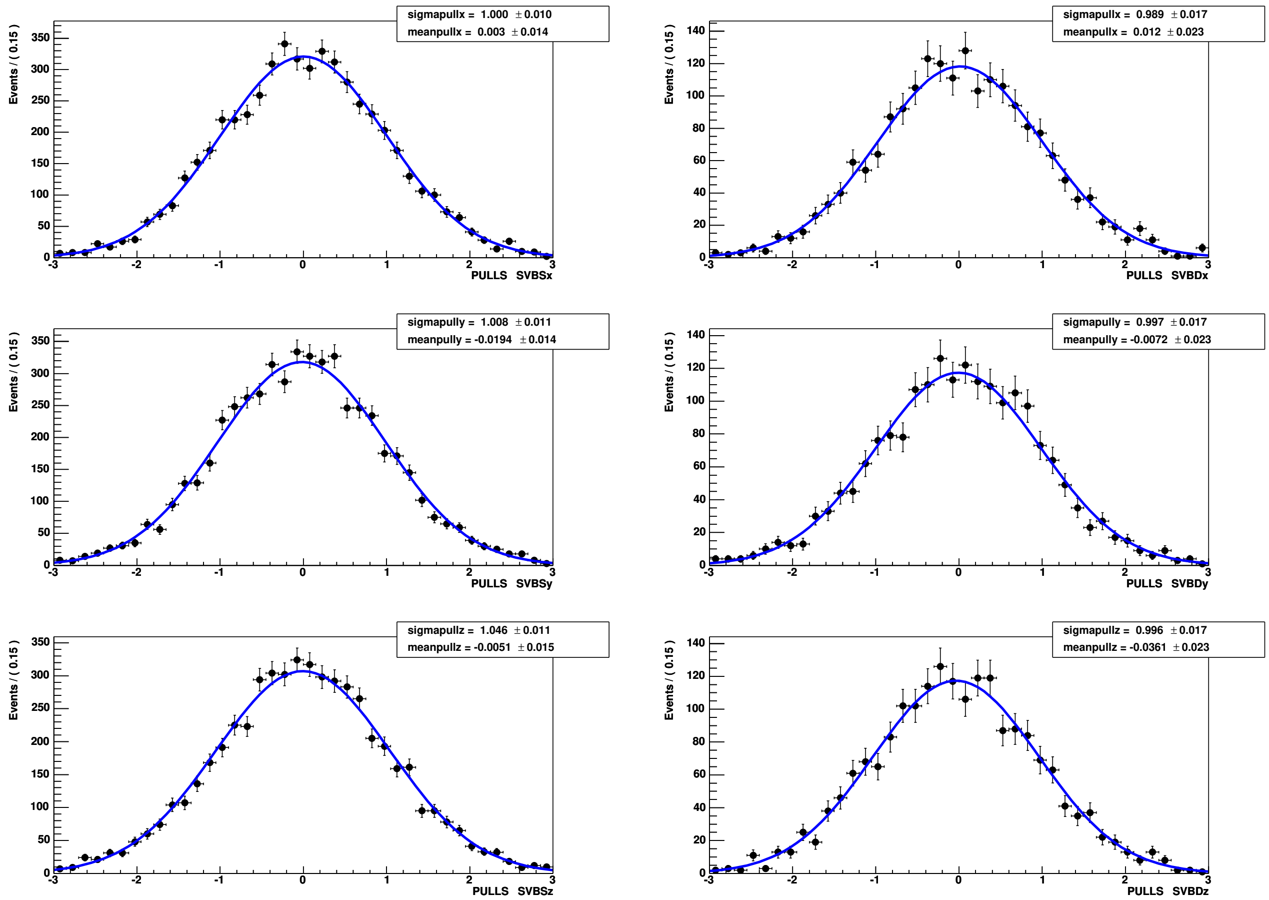

Figure A.6: Secondary Vertex Pulls: (top row) x coordinate, (medium row) y coordinate and (bottom row) z coordinate. left column B_s, right column B_d.

$L_{xy} = \vec{x} \cdot (\vec{p_T}/|\vec{p_T}|)$ and $\vec{x}$ is the vector pointing out from the primary to the secondary vertex. Figure A.7 shows the resolution distributions. We can see from that plot that the mean of the distribution is shifted by 1.1 ± 0.31 microns, for B_s. The pull distributions looks well behaved. We can conclude that the vertexing algorithm is performing very well, and it will be considered as bias free for our measurements. The plots for B_d are also shown in the same figure.

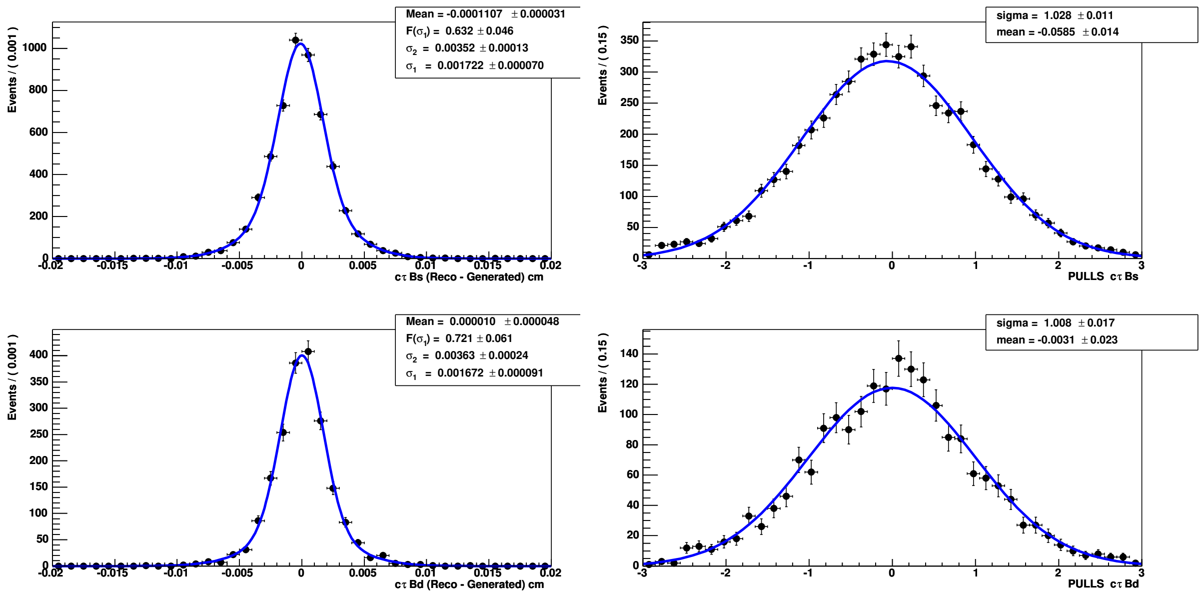

Figure A.7: τ resolution and pulls for B_s (upper) and B_d (lower).

Bibliography

[1] *Measurement of the B_s^0 Lifetime in the Exclusive Decay Channel $B_s^0 \to J/\psi\phi$* Phys. Rev. Lett. 94, 042001 (2005).

[2] "*The Standard Model of Particle Physics*" Mary K. Gallard, Paul D. Grannis, Frank J.Sciully Rev. Mod. Phys.71(1999) **S96-S111**.

[3] "*CP Violation in the renormalizable theory of weak interactions*" Prog. Theor. Phys. **49** , 625-657 (1973).

[4] N. Cabibbo Phys. Rev. Lett. **10** 531, (1963).

[5] L.L Cahu and W.Y. Keung, Phys. Rev. Lett. **53** 1802 (1984).

[6] L. Wolfeinstein, Phys. Rev Lett. **51**, 1945 (1983).

[7] "*The CabibboKobayashiMaskawa quarkmixing matrix*" http:pdg.lbl.gov/2005/reviews/kmmixrpp.pdf

[8] *The BaBar Physics Book: Physics at an Asymmetric B Factory*, ed. P. F. Harrison and H. R. Quinn, SLAC-R-0504.

[9] " *CP Violation*" G. C. Branco, L. Lavoura and J. P. Silva, (Clarendon Press, Oxford, 1999).

[10] " *CP Violation*" I. I. Bigi and A. I. Sanda, (Cambridge University Press, New York, 2000).

[11] *"B decays at the LHC"*, ed. P. Ball *et al.*, hep-ph/0003238 [CERN-TH/2000-101].

[12] V.F. Weisskopf and E.P. Wigner, Z. Phys. **63** (1930) 54; **65** (1930) 18; T. D. Lee, R. Oehme and C. N. Yang, Phys. Rev. **106** (1957) 340.

[13] L.A. Khalfin, Zh. Eksp. Teor. Fiz. **33** (1957) 1371.

[14] Y. I. Azimov, Phys. Atom. Nucl. **59** (1996) 856, and references therein.

[15] "*B physics at the Tevatron RunII and beyond*" K. Anikeev et. al.,FERMILAB-Pub-01/197 (2001). hep-ph/0201071.

[16] S. Abachi, et al., Phys. Rev. Lett. **74** (1995) 2632.

[17] S. Abachi, et al., Phys. Rev. Lett. **79** (1997) 1197.

[18] S. Abachi, et al., Phys. Rev. Lett.**80** (1998) 2063.

[19] S. Abachi, et al., Phys. Rev. **D 58** (1999)052001.

[20] S. Abachi, et al., Phys. Rev. **D 60** (1998) 052001.

[21] V. Abazov, et al., Nature 429 (2004) 638.

[22] '*Three Dimensional Computer Program (TOSCA) for nonlinear electroma gnetic fields*" J. Simkin,C. TrowbridgeRL-79-079 (1979).

[23] See www-d0.fnal.gov/www_buffer/pub/publications for a complete list of DØ publications.

[24] S. Abachi, et al., Nucl. Instrum. Methods Phys. Res. A. 338 (1994) 185.

[25] "*Review of Particles Physics*", S. Eidelman *et al.* (Particle Data Group), Phys. Lett. **B592**, 1 (2004).

[26] M. B. Voloshin and M. A. Shifman, Sov. Phys. JETP **64**, 698 (1986); I. I. Bigi and N. G. Uraltsev, Phys. Lett. **B 280**, 271 (1992); and I. I. Bigi, Nuovo Cimento A **109**, 713 (1996).

[27] "*The Upgraded D0 Detector*", V. Abazov, *et al.* hep-physics/0507191. Submitted to Nucl. Instr. and Methods.

[28] "*The DO object management system: DOom*" $http : //www - d0.fnal.gov/computing/infrastructure/d0om/d0om.html$

[29] An object oriented analysis framework $http : //root.cern.ch/$

[30] standard format for Monte Carlo generators output $http : //cepa.fnal.gov/psm/stdhep/$

[31] GEANT detector description and simulation tool $http : //wwwasd.web.cern.ch/wwwasd/geant/$

[32] $http : //d0server1.fnal.gov/users/nomerot/Run2A/BANA/Dskim.html.$

[33] "B_s *lifetime analysis web page* $http : //www - d0.fnal.gov/cinvestav/d0_private/Analysis/Bs/Bs.html$

[34] D. J. Lange, Nucl. Instrum. Meth. **A462**, 152, (2001); for details of the decay models in the package, please see $http : //www.slac.stanford.edu/ lange/EvtGen.$

[35] The official production Monte Carlo site is located at:

$http : //www{-}d0.fnal.gov/Run2Physics/ckm/d0\_private/computing/mc\_files.html$,

Details of the request can be obtained from:

$http : //www - d0.fnal.gov/computing/mcprod/request\_details/Request\_id$

where id, is the official request id: 11784, 11832 and 10983.

[36] $http : //d0server1.fnal.gov/users/nomerot/Run2A/B\_ANA.html$

[37] "*b*-tagging in DELPHI at LEP", DELPHI Collaboration, *Eur. Phys. J.* **C32** (2004), 185-208.

[38] Offline Run Quality Database, $http : //d0db.fnal.gov/qualitygrabber/qualQueries.html.$

[39] "Good and Bad Muon Global "; D0 Note 3939; H. T. Diehl, V. M. Abazov, and R. McCroskey; 2002.

[40] "Studies of $\Upsilon(1S)$ bottomonium state production with the DØ Detector at Fermilab"; D0 Note 4264; D. Bauer, J. Huang and A. Zieminski; 2004.

[41] "*Inclusive B lifetime at DØ*", E. Cruz-Burelo, DØ Note 4257

[42] "*Charged B lifetime at DØ*", P. Podesta, DØ Note 4273

[43] Geometry Files where provided by A. Sopczak:
$clued0 : /home/sopczak/ricksgeometries$
Shifts on the SMT geometry were suggested by the alignment group.